

# Complementary Shear Banding During Warm Rolling of Alloy 625 Leads to Uncharacteristic Development of $\gamma$ -Fiber Texture



ASHWIN KUMAR GODASU, SUMEET MISHRA, UJJWAL PRAKASH, ARUNANSU HALDAR, and SUHRIT MULA

In the present study, we propose a novel interpretation of  $\gamma$ -fiber  $\langle 111 \rangle \parallel \text{ND}$  development during warm rolling of superalloy 625 solely based on reaction stresses generated across the shear bands (SBs) in contrast to the typical twin rotation mechanism suggested in low-SFE materials. Alloy 625 develops a weak Cu-type texture up to intermediate rolling stages with planar dislocation slip as the dominant deformation mechanism. Thereafter, a drastic shift in the deformation mode from the planar slip to extensive non-crystallographic shear banding is observed. The micro-SBs that primarily originated in Cu-oriented grains have extended into neighboring grains upon further deformation and some of them ceased only after reaching the sample scale. Moreover, concurrent nucleation of new sets of complementary micro-SBs ( $\pm 30$  to  $40$  deg) has subdivided the grains into rhomboidal fragments. At large strains, the sample scale SBs experience reaction stresses caused by roller contacts and undergo rigid body rotations toward compression plane. This mechanism has contributed to further mesoscopic shearing along micro-SBs and change in orientation of adjacent matrix regions. Furthermore, we find that the geometry of reaction stresses developed across complementary micro-SBs has manifested in strain path change of entrapped grain fragments from plane strain to pure shear, leading to the development of  $\gamma$ -shear fiber. The textural changes induced by shear banding are comprehended by microstructural investigations (through SEM-EBSD & TEM) and crystal plasticity simulations.

<https://doi.org/10.1007/s11661-023-07275-7>

© The Minerals, Metals & Materials Society and ASM International 2023

## I. INTRODUCTION

NICKEL-BASED superalloy 625 is a solid solution strengthened alloy consisting of 35 to 40 wt pct of solute, of which Cr, Mo, and Nb are the major constituting elements. The composition of this alloy is adjusted in a way to impart high-temperature strength alongside excellent oxidation and corrosion resistance.<sup>[1]</sup> Owing to the significant work-hardening capacity of alloy 625, its plastic deformation behavior is usually studied under hot and warm working conditions.<sup>[2–4]</sup> However, deformation micromechanisms operating in

alloy 625 during warm deformation and their correlation with microstructural features such as micro- & macroscale shear bands (usually observed in concentrated solid solution alloys<sup>[5–8]</sup> at intermediate to later stages of deformation) are lacking in the literature. It is well known that crystallographic texture carries the signature of deformation micromechanisms.<sup>[9]</sup> Therefore, systematic tracking of crystallographic texture evolution as a function of plastic strain could establish the interconnection between the active deformation modes and microstructural development in alloy 625.

In most cases, the texture evolution in FCC materials during plastic deformation is directly linked to the material's stacking fault energy (SFE), *i.e.*, on the extent of cross-slip of dislocations.<sup>[5–12]</sup> Accordingly, two different kinds of rolling texture formation in FCC materials are reported: (1) Copper (Cu) type in medium-to-high-SFE materials that consists of equally intense Cu  $\{112\}\langle 111 \rangle$ , Bs  $\{110\}\langle 112 \rangle$ , and S  $\{123\}\langle 634 \rangle$  components; and (2) Brass (Bs) type in low-SFE materials with strong Bs and Goss  $\{110\}\langle 100 \rangle$  components. Several theories have been developed to comprehend the texture transition from Cu type to Bs

ASHWIN KUMAR GODASU, SUMEET MISHRA, UJJWAL PRAKASH, and SUHRIT MULA are with the Department of Metallurgical and Materials Engineering, IIT Roorkee, Roorkee 247667, India. Contact e-mail: [suhrit.mula@mt.iitr.ac.in](mailto:suhrit.mula@mt.iitr.ac.in) ARUNANSU HALDAR is with the Suresh Gyan Vihar University, Mahal, Jagatpura, Jaipur 302017, India.

Manuscript submitted April 6, 2023; accepted November 23, 2023.  
Article published online December 28, 2023

type.<sup>[12–14]</sup> Dillamore *et al.*<sup>[12]</sup> have proposed the cross-slip theory, where intensity & stability of Bs orientation are defined based on extent of the cross-slip. In another attempt, Wassermann *et al.*<sup>[13]</sup> suggested a positive role of deformation twinning in near Cu-oriented grains on final Bs-type texture evolution. The twinning shear would generate twinned Cu {552}<115>-oriented regions, which further undergo normal slip to rotate toward metastable Goss and finally to Bs orientation. Correspondingly, some of the studies have incorporated twinning system {111}<112> in simulations for predicting rolling texture and were successful in tracking the observed texture transition.<sup>[15,16]</sup> However, later experimental investigations have shown that the volume percentage of twins is too low to affect the overall texture and most importantly, their evolution stagnates after a certain amount of deformation.<sup>[14]</sup> Instead, Leffers *et al.*<sup>[11,14]</sup> suggested that selective coplanar slip parallel to twin lamellae inside the grains due to latent hardening of other intersecting slip systems could better explain the obtained crystal rotations and subsequent Bs-type texture formation.

Irrespective of SFE, microstructural investigations of concentrated solid solution alloys of Cu–Zn,<sup>[5]</sup> Cu–Mn,<sup>[6]</sup> Ni–Co,<sup>[7]</sup> and austenitic stainless steel<sup>[8]</sup> have revealed the presence of extensive shear bands (SBs) from intermediate to higher rolling reductions. SBs generate as a consequence of non-uniform accumulation and migration of dislocations during plastic flow, which corresponds to a state where the material experiences local plastic instability ( $d\sigma/d\varepsilon \leq 0$ ).<sup>[17,18]</sup> Two types of SBs have been reported, namely Cu type and Bs type.<sup>[11]</sup> The difference arises from pre-existing dislocation structure responsible for resisting further dislocation movement. Cu-type SBs develop in medium-to-high-SFE materials where prior dislocation cell walls resist dislocation movement, and Bs-type SBs form in low-SFE materials, where the resistance is offered by pre-existing deformation twin stacks. Due to significant shear banding observed in solid solution alloys, their presence is often held responsible for the observed Cu to Bs-type texture transition via latent hardening effects. The role of short-range ordering (SRO) in promotion of planar dislocation slip and subsequent shear banding in solid solution alloys was investigated by Engler<sup>[6]</sup> using Cu–Mn alloy as a model material. It was observed that SRO becomes prevalent after 8 pct of Mn concentration, which advanced the onset of shear banding and resulted in Cu to Bs-type texture transition. In another study, although no SRO was observed by Madhavan *et al.*<sup>[7,19]</sup> in Ni–40 pct Co alloy, still the grain scale micro-SBs were observed after an extremely large reduction (98 pct) possibly due to the exhaustion of active slip systems. Moreover, it is reported that there is subgrain development via dynamic recovery within SBs and they are preferentially oriented toward Goss. Consequently, the shift of intensity toward Goss position has accounted for the texture transition. The progressive recovery-mediated dislocation arrangement inside SBs is attributed to lower solute strengthening offered by Ni–Co alloys owing to a marginal misfit in

atomic size of Co and Ni atoms. Therefore, both solute concentration and nature of solute elements influence deformation microstructure and resulting texture evolution. Overall, shear banding could be considered as an ultimate mode of deformation when further work hardening is not sustained by FCC materials under rolling conditions.

The above studies suggest that inhomogeneous deformation due to micro- or macroscale shear banding plays an important role in controlling crystallographic texture evolution of concentrated solid solution alloys like superalloy 625. Therefore, for elucidating the underlying deformation micromechanisms in alloy 625, it is necessary to characterize the microstructure at different levels of plastic deformation and correlate it with crystallographic texture evolution. In this regard, the current study investigates the microstructure and texture changes in alloy 625 through X-ray diffraction and optical/electron microscopy techniques. The investigation focuses on various warm rolling reductions up to a true strain of 2.3 (about 90 pct reduction). The experimental work is further supplemented by crystal plasticity simulations using the viscoplastic self-consistent (VPSC) model.

## II. MATERIALS AND METHODS

### A. Material & Warm Rolling Schedule

Ni-based superalloy 625 in the as-cast state is provided by MIDHANI Ltd., Hyderabad, India. The average alloy composition as obtained from energy-dispersive X-ray spectroscopy (EDS) analysis is 62.3Ni, 22.8Cr, 8.98Mo, 3.84Nb, 0.54(Al + Ti), and 1.51(Fe + Si). The alloy was homogenized and subsequently hot-rolled at 1150 °C to produce a recrystallized grain structure. The hot-rolling schedule was according to the best working zone established from hot compression studies of the same alloy reported in our previous work.<sup>[3]</sup> Rectangular slabs of size 30 × 15 × 6.5 (all in mm) were cut from the hot -rolled plate using a wire-electric discharge machine (EDM) and were then subjected to warm rolling at 500 °C. The warm rolling temperature was chosen in a way not to incur any precipitation during rolling. The samples were unidirectionally rolled up to three thickness reductions of 30, 60, and 90 pct, corresponding to a true strain ( $\varepsilon_i$ ) of approximately 0.36, 0.92, and 2.3, respectively. The desired thickness is achieved by applying a rolling schedule with each pass consistent with a true strain of 0.105. The experiment was conducted using a 4-high rolling mill featuring work rolls having 65 mm diameter and operating at a constant angular velocity of 8.5 rpm.

### B. Microstructure and Texture Characterization

Microstructure at different rolling reductions was characterized by optical, scanning, and transmission electron microscopy (SEM & TEM). Orientation imaging microscopy (OIM) of the rolled samples was carried out in Zeiss Gemini FE-SEM equipped with an electron

backscatter diffraction (EBSD) detector. The EBSD scans of deformed samples were taken from the transverse plane (RD-ND) and rolling plane (RD-TD). The required surface finish of samples was attained by emery-paper polishing followed by electropolishing in a solution containing 20 pct perchloric acid in methanol maintained at 5 °C to 10 °C. The scans were obtained using a step size of 0.2  $\mu\text{m}$  for 30 and 60 pct rolled samples. For a 90 pct rolled sample, a finer step size of 60 nm was used. Post-processing analysis of scanned data was carried out in the TSL-OIM software. Samples for optical microscopy were prepared by electrolytic etching in Lucas's reagent (50 mL lactic acid + 150 mL HCL + 3 g oxalic acid) at 1.6 V for 10 seconds. Further, dislocation structures and their characteristics in the rolled samples were studied using JEM 3200FS HR-TEM operated at 300 kV. The TEM samples were prepared using a twin-jet electropolishing unit; experimental details are discussed elsewhere.<sup>[20]</sup>

The bulk texture of rolled samples is measured on the RD-TD plane at the mid-thickness level to avoid any shear deformation caused by friction generated between sample surfaces and the rollers. A near plane strain condition is mostly achieved at this mid-section level. Texture measurements were carried out by collecting three incomplete pole figures (111), (200), and (220) using an X-ray goniometer (Rigaku SmartLab) with Cu K-alpha radiation. The measured incomplete pole figures are then post-processed by importing them into MATLAB toolbox—MTEX to compute the orientation distribution function (ODF). Ghost correction was performed on pole figure data for calculating ODF. The MTEX is a free open-source software that allows to analyze and model texture deduced from the experimental EBSD/pole figure data.<sup>[21]</sup> The ODF plots project the frequency of orientations occurring in 3D Euler space, which describes the three consecutive rotations ( $\varphi_1, \varphi, \varphi_2$ ) required to align the crystal axis along the specimen axis. In the present work, as rolling experiments were conducted unidirectionally, the ODF plots are generated by imposing orthotropic specimen symmetry. Throughout the article, texture is represented by plotting ODF  $\varphi_2$  sections = 0, 45, and 65 deg, as most of the deformation texture components developed during rolling of FCC material can be identified on these  $\varphi_2$  sections.<sup>[9,18]</sup> The texture intensities displayed on ODF plots are represented as multiples of a random distribution (m.r.d.).

### C. Texture Simulation

The Viscoplastic self-consistent (VPSC) model is used in the present study to simulate the experimental rolling textures. The VPSC model accounts for the anisotropic deformation behavior of individual grains inside a polycrystalline medium when subjected to high strains and strain rates. It achieves this by defining each grain as an inhomogeneous ellipsoidal inclusion embedded inside a homogenous equivalent medium (HEM) carrying average properties of the polycrystalline aggregate.

The model allows each grain to deform differently by considering certain linearization schemes to describe relative stiffness of the grain with respect to the HEM. Lastly, the VPSC model relies on the fact that iterations are performed at each step of the simulation such that self-consistency is maintained as described in Figure 1(a). It was first proposed by Molinari *et al.*<sup>[22]</sup> and a further full mathematical model was established by Lebensohn and Tome.<sup>[23]</sup> Details of mathematical approach adopted in the VPSC model are provided in the appendix.

Initially, VPSC simulations were performed to identify the single crystal Voce hardening parameters ( $\tau_0, \tau_1, \theta_0, \theta_1$ ) of alloy 625. This is achieved by establishing a decent fit between the simulated Von Mises stress-strain curve and the experimental flow stress curve recorded from a uniaxial compression [Figure 1(b)]. The compression experiment was carried out in a Gleeble 3800 thermomechanical simulator at 500 °C with 1/s strain rate using a cylindrical sample of 6 mm diameter and 9 mm length (the deformation conditions are similar to that adopted in warm rolling). VPSC simulations are performed using the intermediate interaction scheme ( $n^{\text{eff}} = 10$ ) by imposing a compression velocity gradient tensor as specified in Figure 1(b). The input texture used for simulation studies was obtained by discretizing the ODF of initial base material to 5000 single orientations. All simulations were run by enforcing deformation in incremental steps of 0.01 up to the desired true strain. Values of hardening parameters corresponding to the best fit are indicated in Figure 1(b). These parameters are then utilized throughout the study to describe the self-hardening behavior of octahedral slip systems while simulating the rolling texture.

## III. RESULTS

### A. Microstructure and Textural Characteristics of the Base Material

Microstructure and texture of the hot-rolled base material are indicated in Figure 2. The microstructure reveals the presence of equiaxed recrystallized grains with a higher density of annealing twin boundaries ( $\sim 52$  pct as obtained from orientation imaging). Statistical grain size of the base material measured using ImageJ software by excluding twin boundaries is around  $82 \pm 30 \mu\text{m}$ . The material also contains carbide particles that were developed primarily during casting<sup>[3]</sup> and remained undissolved upon further homogenization/hot rolling. Nevertheless, these carbide particles get redistributed into banded structures during hot rolling. These bands are visible on the transverse section as they have formed in planes parallel to the plate surface [Figure 2(b)]. Coming to the initial texture, the ODF sections indicated in Figure 2(d) represent the presence of near-random texture in the base material (Max intensity: 1.6 m.r.d.), which is a consequence of dynamically recrystallized grain structure developed during hot rolling.<sup>[18]</sup>

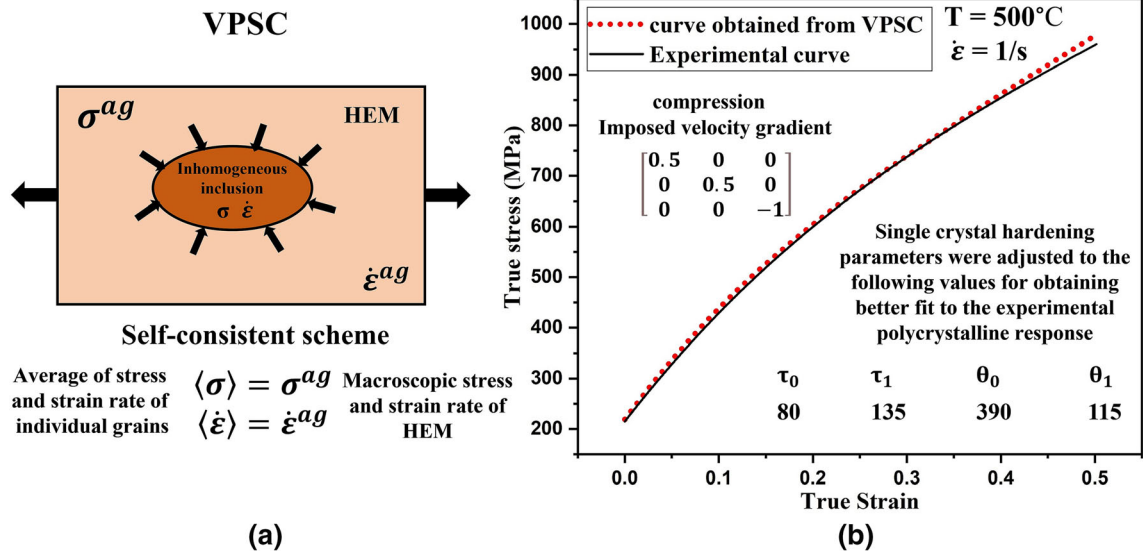


Fig. 1—(a) Representation of the VPSC formulation, (b) VPSC simulation is run to adjust single crystal hardening parameters for obtaining a better fit to the experimental stress–strain curve of alloy 625 obtained from uniaxial compression testing in Gleeble simulator. (Test temperature and strain rate are similar to the rolling conditions adopted.).

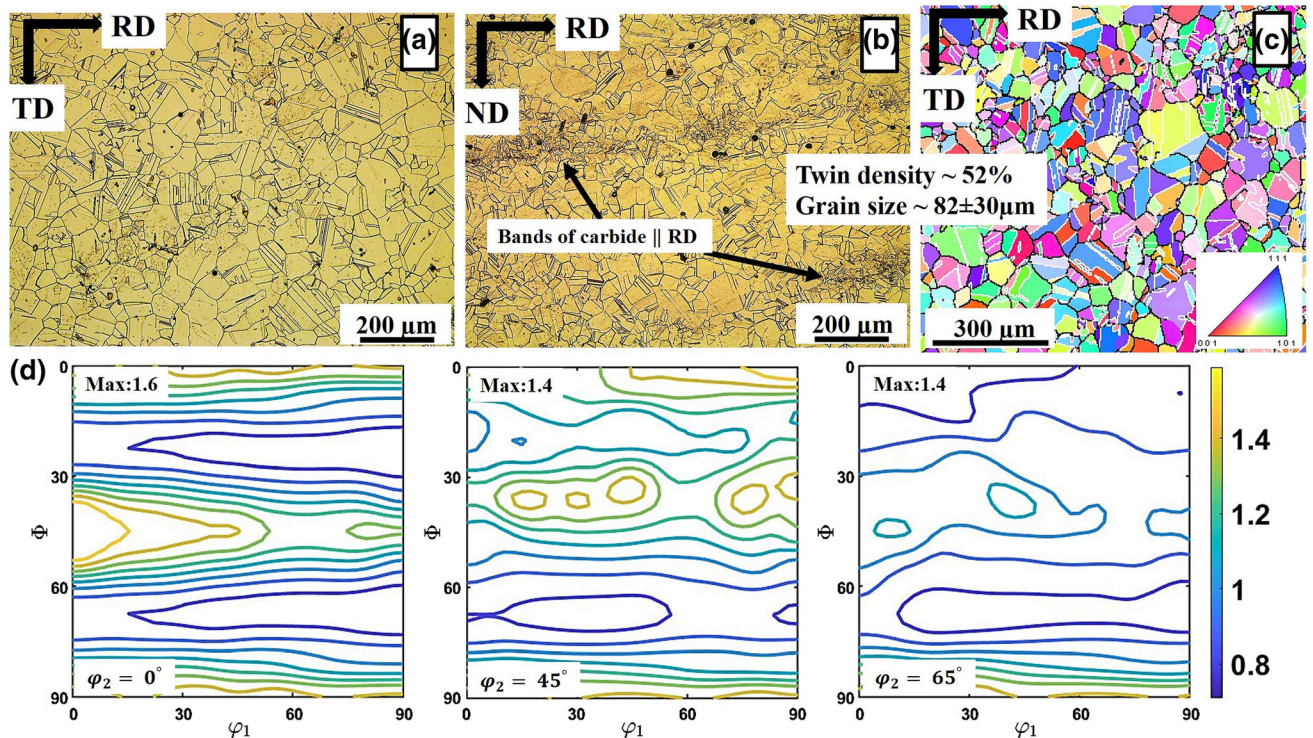


Fig. 2—Microstructural characteristics of the base material. (a) and (b) Optical micrographs captured from RD-TD and RD-ND planes. (c) Inverse pole figure map (twin boundaries are marked with white). (d) ODF  $\phi_2$  sections 0, 45, and 65 deg show nearly random texture (max intensity: 1.6 m.r.d.) exhibited by the base material (textural studies were carried out on RD-TD plane at mid-thickness level).

### B. Deformation Texture Evolution in Studied Alloy 625

The ODF sections  $\phi_2 = 0, 45,$  and  $65$  deg of all the warm-rolled samples are shown in Figure 3. The positions of main deformation texture components developed are labeled, and the corresponding Miller indices are listed in Table I. It can be noticed from the

ODF plots that alloy 625 displays a signature of Cu-type texture up to 60 pct rolling reduction [Figures 3(a, b)]. Correspondingly, there was a gradual rise in the texture intensity for all the major FCC rolling components. However, the texture strengthening is sluggish as the maximum intensity of only 3.3 m.r.d is obtained even after 60 pct rolling reduction. Thereafter, the increase in

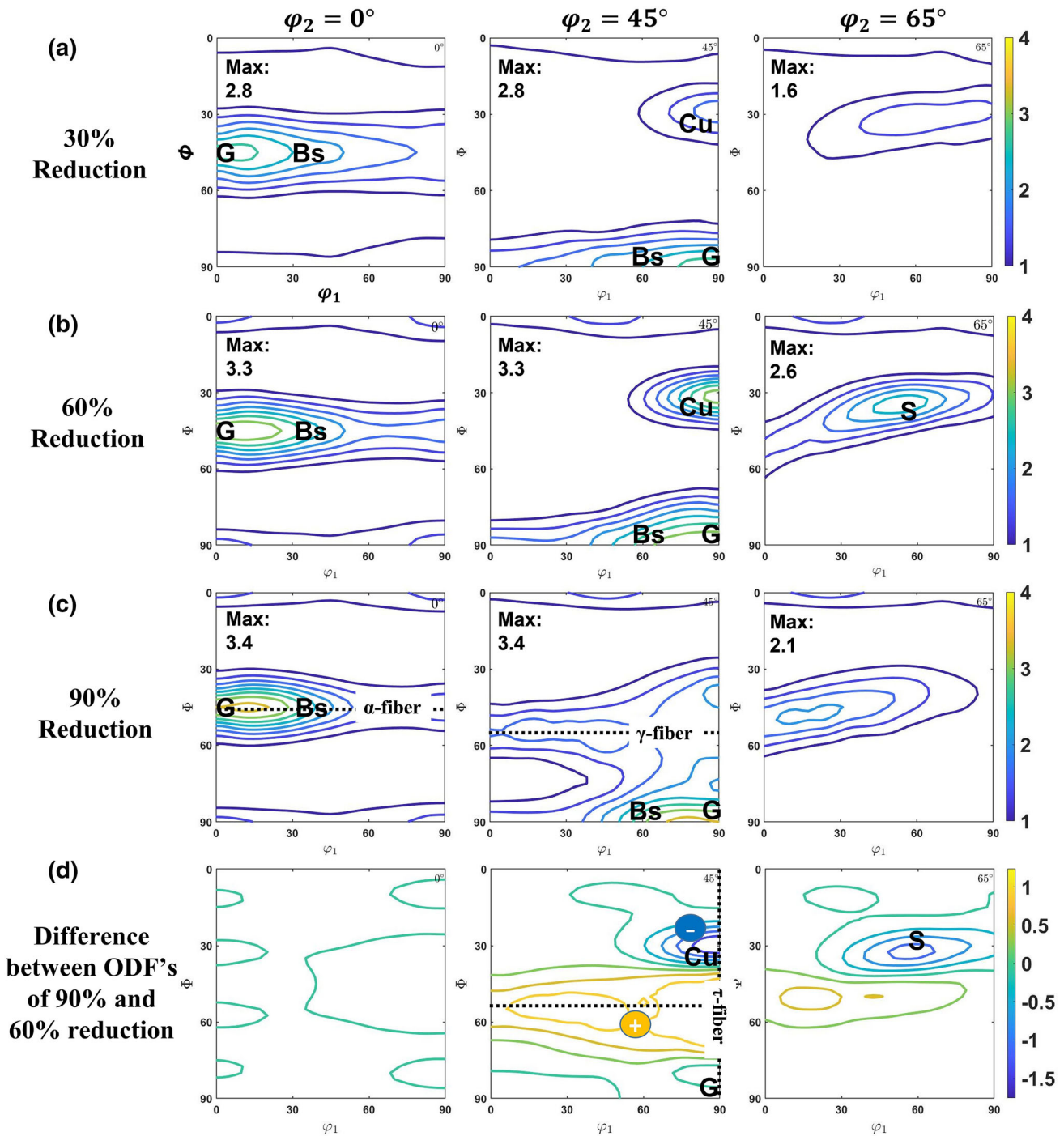


Fig. 3— $\varphi_2 = 0^\circ$ ,  $45^\circ$  and  $65^\circ$  ODF sections plotted from experimental bulk texture obtained at different rolling reductions: (a) 30 pct, (b) 60 pct, and (c) 90 pct. The difference in ODF's of 90 and 60 pct reduction samples are plotted in (d).

**Table I. Euler Angles of Different FCC Deformation Texture Components Representing Their Position in 3D Euler Space (Under Orthorhombic Specimen Symmetry)<sup>[9]</sup>**

Deformation $\{hkl\} \langle uvw \rangle$	Texture	Components	Cu $\{112\} \langle 111 \rangle$	Bs $\{110\} \langle 112 \rangle$	S $\{123\} \langle 634 \rangle$	Goss $\{110\} \langle 001 \rangle$	Shear $\{111\} \langle 112 \rangle$
Euler Angles $\varphi_1, \varphi, \varphi_2$ in Degrees (Bunge Notation)			90, 35, 45	35, 45, 0	59, 36.7, 63	0, 45, 0	90, 55, 45

rolling reduction to 90 pct has not much contributed to further texture sharpening as the maximum intensity has only raised to 3.4 m.r.d. Additionally, the ODF sections of the 90 pct rolled sample [Figure 3(c)] also indicated an occurrence of texture transition represented by the loss in texture intensity around Cu and S positions. The loss/redistribution of intensity could be better visualized by plotting the difference between the ODFs of 90 and 60 pct rolled samples [Figure 3(d)]. The difference plot indicates that the loss in the intensity of Cu orientation has not much influenced the texture intensity of existing Goss or Bs orientations; instead, there is a new texture intensity evolved along the  $\gamma$ -shear fiber ( $\{111\}||ND$ ). The axis along  $\varphi_1$  at constant  $\varphi = 55$  deg depicted in the ODF  $\varphi_2 = 45$  deg section [Figure 3(c)] is known as  $\gamma$ -fiber.<sup>[9]</sup> The observed shear texture evolution is unnatural for FCC materials to develop under plane strain conditions. It is reminded again that texture data were collected from the mid-thickness section, where shear effects from friction and roll gap geometry are negligible.

To further emphasize the texture evolution during warm rolling, the classical  $\beta$  and  $\tau$ -fibers used for studying texture transitions in FCC materials are plotted in Figure 4. The fiber texture plots quantitatively assess variation in texture intensity/orientation density ( $f(g)$ ) along an axis connecting various texture components.<sup>[9]</sup> The  $\beta$ -fiber elucidates  $f(g)$  distribution over the orientation path connecting Cu, S, and Bs components, which is the axis inclined at 60 deg from ND toward RD and running along  $\varphi_2 = 45$ –90 deg.<sup>[5,9]</sup> From the  $\beta$ -fiber plot [Figure 4(a)], it can be seen that there is a gradual evolution of  $f(g)$  of Cu and Bs components up to 60 pct reduction. However, upon an increase in rolling reduction from 60 to 90 pct, there is no clear evidence of texture intensity shift from Cu to Bs position

as reported previously in the case of concentrated solid solution alloys.<sup>[5,6,8]</sup> Instead, texture intensity decreases at both Cu and Bs positions after 90 pct rolling reduction. The trend is similar for the S component but with marginal intensity changes. The Cu and Goss orientations indicated in the ODF section  $\varphi_2 = 45$  deg are connected through the  $\tau$ -fiber that runs along  $\varphi$  at constant  $\varphi_1 = 90$  deg.<sup>[9]</sup> The  $\tau$ -fiber plot [Figure 4(b)] indicates that there is no change in texture intensity at the Goss position from 60 to 90 pct rolling reduction. Nonetheless, there is a significant decrease in texture intensity at the Cu position accompanied by a simultaneous rise at  $\varphi = 55$  deg position, which correspond to the  $\{111\}[112]$  shear texture component.

### C. Microstructural Characterization of Deformed State at Different Rolling Reductions

The inverse pole figure (IPF) map and the grain reference orientation deviation (GROD) map plotted from the EBSD data of 30 pct rolled sample are shown in Figures 5(a) and (b), respectively. The micrographs indicate significant orientation deviation inside the grains with no observable deformation twinning. Measure of the deviation can be recorded from the GROD map [Figure 5(b)], which gives misorientation of each pixel inside a grain with respect to the grain average orientation. It could be seen that misorientation builds from the grain interior toward the grain boundary, with a sharp rise observed in regions closer to the boundary. These regions are usually known as grain boundary-affected zones (GBAZ).<sup>[24,25]</sup> During deformation, complex lattice rotations near grain boundaries to ensure compatibility between neighboring grains lead to development of large-scale misorientations. An extreme case is shown in Figure 5(b), where a misorientation as high

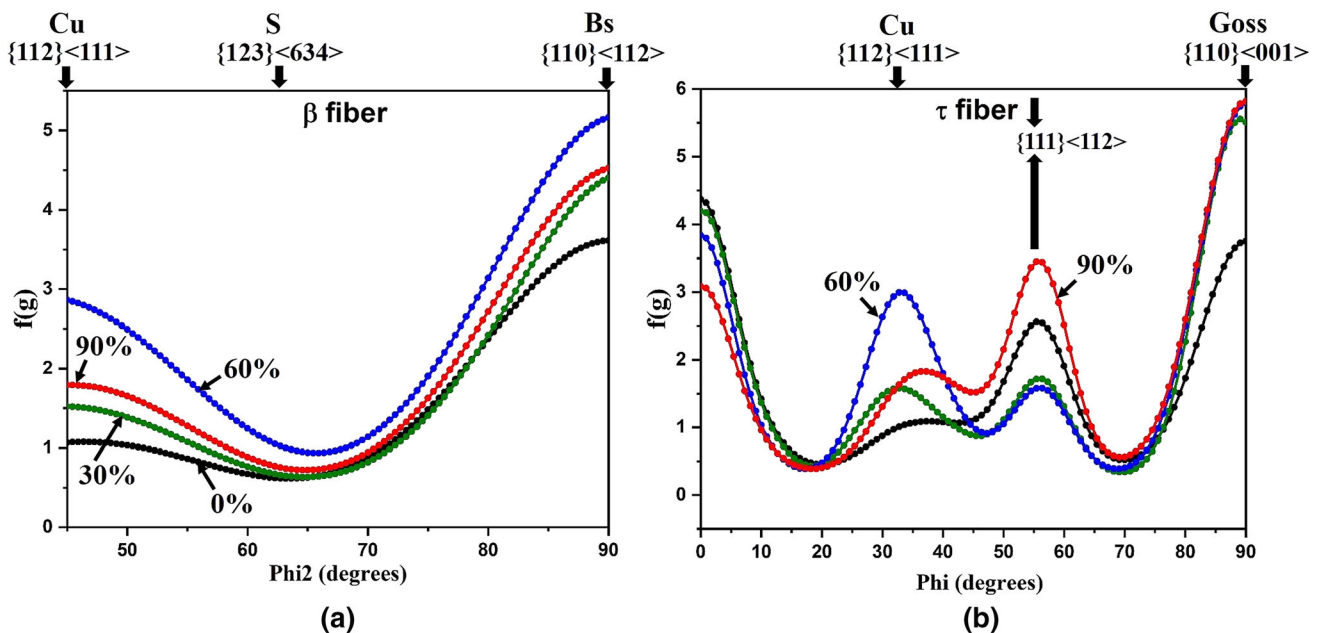


Fig. 4—Comparison of texture fiber plots at different rolling reductions, (a)  $\beta$ -fiber and (b)  $\tau$ -fiber. Different positions of deformation texture components along the fiber are indicated.

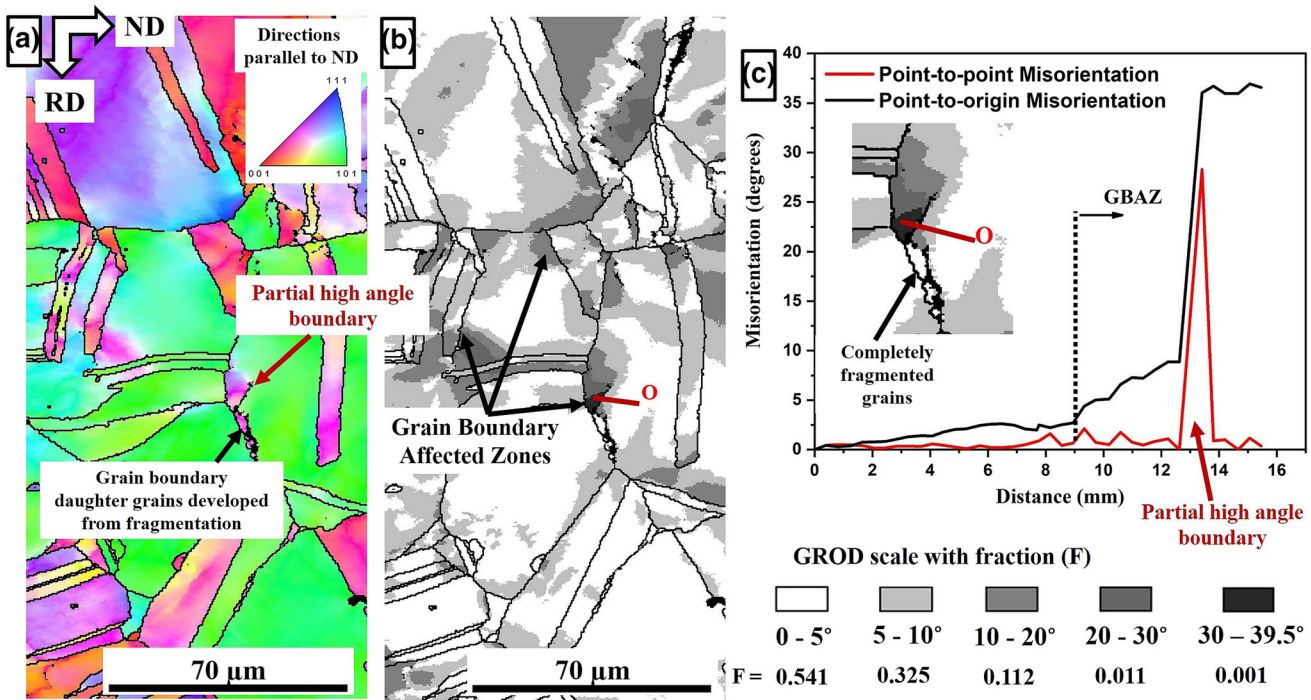


Fig. 5—OIM micrographs of sample rolled to 30 pct reduction, (a) Inverse pole figure map superimposed by high-angle grain boundaries, (b) Grain Reference Orientation Deviation (GROD) map indicating the generation of higher misorientations near grain boundaries (scale bar is given beside the map). (c) Point-to-point and point-to-origin misorientation between neighboring pixels along line O marked red in the GROD map as shown in the insert (Color figure online).

as 38 deg is observed for one of the GBAZ regions. Development of such high misorientations is usually accommodated by generation of geometrically necessary dislocations (GNDs) that address local lattice curvature and by the formation of geometrically necessary boundaries (GNBs) that account for large strain heterogeneities.<sup>[26,27]</sup> The point-to-point and point-to-origin misorientation profiles along line O marked on the GROD map [Figure 5(c)] indicate emergence of a partially developed new high-angle (~ 28 deg) boundary in the above-mentioned GBAZ region. Building of new GNBs by more and more accumulation/storage of GNDs during ongoing deformation would ultimately result in grain fragmentation.<sup>[27,28]</sup>

After 60 pct rolling reduction, there is an increase [Figures 6(a) and (b)] in fraction of deformation heterogeneities such as irregular low-angle GND boundaries, fragmented grains, and heavily strained/lattice-distorted regions. Most of these heterogeneities are developed in the vicinity of grain boundaries and carbide particle band regions as a result of inhomogeneous plastic strain accommodation. Moreover, it is noticed that advent of grain elongation and fragmentation is pronounced near carbide particle bands and the corresponding zone extends to larger volumes [marked in Figure 6(b)]. Apart from aforementioned structures, the microstructure also revealed the presence of ~ 35 deg sharp band-like features within some of the grains. Based on their geometrical inclination to RD, these parallel bands are identified as micro-SBs that represent intense plastic strain-localized regions formed

by a non-crystallographic slip of dislocations.<sup>[17,29]</sup> Furthermore, some of the micro-SBs can be seen extending into adjacent grains [Figure 6(a)], suggesting that they could be converted into macroscale SBs upon subsequent rolling reductions. Crystal orientation map shown in Figure 6(c) indicates that microshear band formation is primarily taking place inside the grains having Cu orientation [region 1 in Figure 6(d)]. This is a common observation because it is well known that Cu orientation inherently suffers from shear banding due to its asymmetrical slip distribution on equally stressed slip systems.<sup>[30]</sup> On the other hand, some of the grains with near Bs orientation are seen to develop Goss-oriented deformation band regions near the grain boundaries [region 2 in Figure 6(d)]. Deformation bands are usually generated as a consequence of activation of a different set of slip systems across the grain.<sup>[18]</sup>

Figure 7 shows microstructure and microtextural characteristics of the sample rolled to 90 pct reduction. Optical micrograph [Figure 7(a)] depicts large-scale development of complementary SBs at different length scales (micro-, macro-, and sample scale). The positive and negative SBs inclined at 30 to 40 deg to RD have subdivided the grains into distorted rhomboidal prism regions, whose axis is parallel to TD [Figure 7(b)]. Such intense banded structure usually develops due to continuous generation and extension of micro-SBs into neighboring grains to form macro- and sample scale SBs. The significant rise observed in shear band volume after 90 pct rolling reduction implies that after intermediate rolling stages, the deformation is dominated by

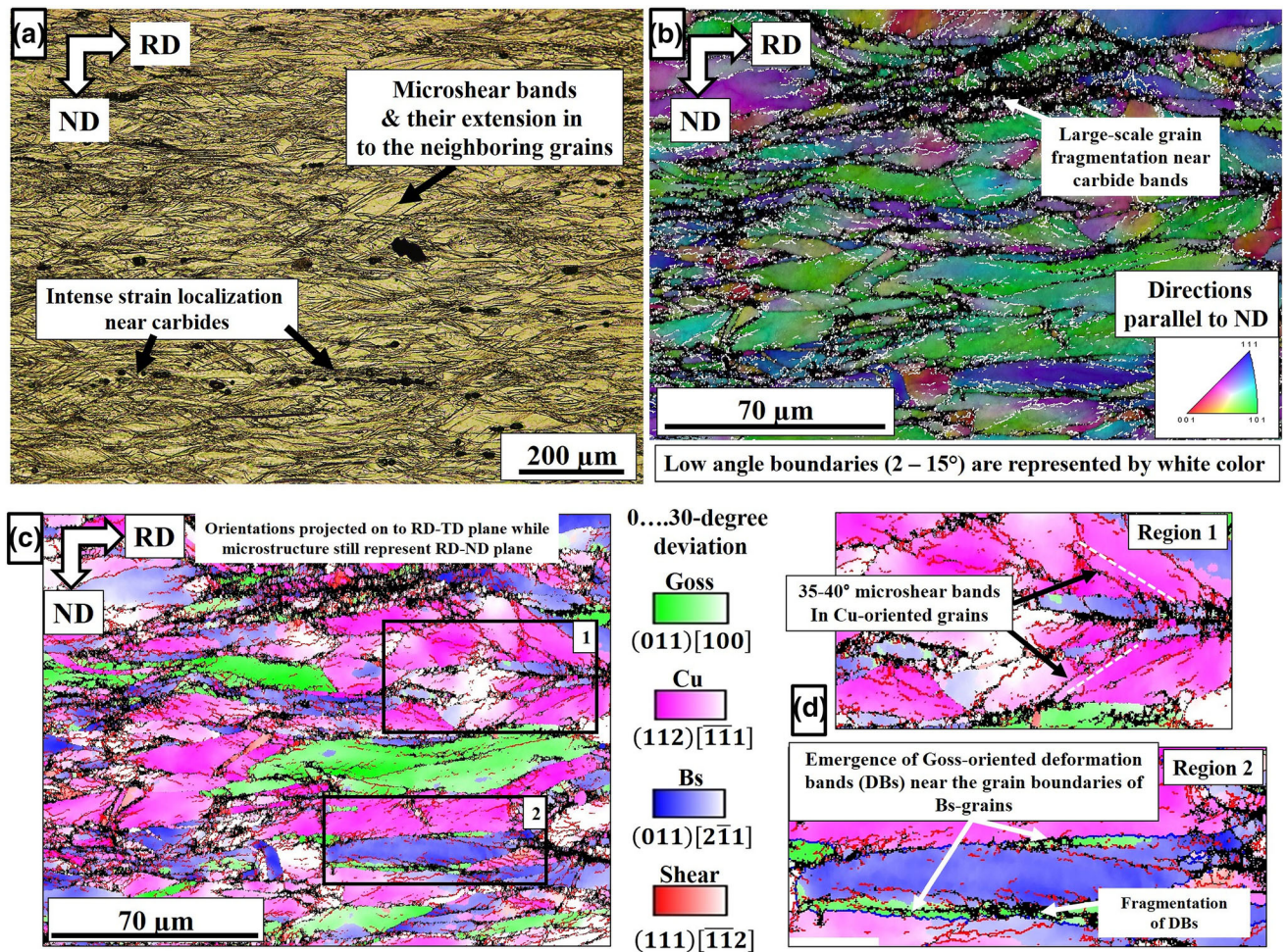


Fig. 6—Microstructure and microtextural features of the sample rolled to 60 pct thickness reduction. (a) Optical micrograph, (b) Inverse pole figure map superimposed on the band contrast image (low-angle boundaries are marked in white), (c) crystal orientation map presented on RD-TD plane with different components represented by the given color code aside (here, microstructure still represents RD-ND plane), (d) Enlarged view of the regions 1 and 2 marked in (c) demonstrating the development of two kinds of microstructural inhomogeneities at grain scale after 60 pct rolling, one at the grain boundaries and other in Cu-oriented grains (Color figure online).

intense dislocation movement along shear band planes in the band direction.

Figures 7(c) and (d) show the crystal orientation map and its enlarged view, which describes local textural distribution in and around the SBs. After 90 pct reduction, it has been observed that SBs are not limited to Cu-oriented grains, but have also spread into Bs-oriented neighbors as a result of their propagation to the sample scale. In contrast, Goss orientation has shown more resistance to shear banding. Moreover, neighboring Cu-oriented matrix regions enclosed between complementary SBs undergo lattice rotations toward the shear orientations [Figures 7(c) and (d)]. The (111) pole figure [Figure 7(e)] represents  $-20$  deg TD rotation of Cu (112)[111] regions toward (111)[112] shear orientation. The developed shear components also undergo some degree of rotation around ND, producing orientations spread along the  $\gamma$ -fiber ( $\langle 111 \rangle \parallel \text{ND}$ ). These microtextural observations are coherent with the macrotexture results. Here, (111) pole figure is plotted after partitioning out regions with Cu and shear orientations

from the total orientation data considering a 30 deg tolerance. Coming to orientations inside SBs, a major part of the bands show non-indexed portions with a small fraction of Goss-oriented crystals engulfed inside them [Figure 7(d)].

#### D. Grain Misorientation Distributions

The difference between correlated (based on first neighbors) and uncorrelated (based on random neighbor) grain misorientation angle distributions has been used to understand the mode of deformation.<sup>[31]</sup> It is reported that if correlated and uncorrelated grain misorientation distributions more or less coincide, deformation follows the upper-bound Taylor's model with no evolution of GNDs. However, an increase in disparity between these distributions would suggest that deformation is occurring more heterogeneously and at a higher deviation, it can be said that the deformation is moving toward the lower bound Sachs-type deformation (single slip activity).



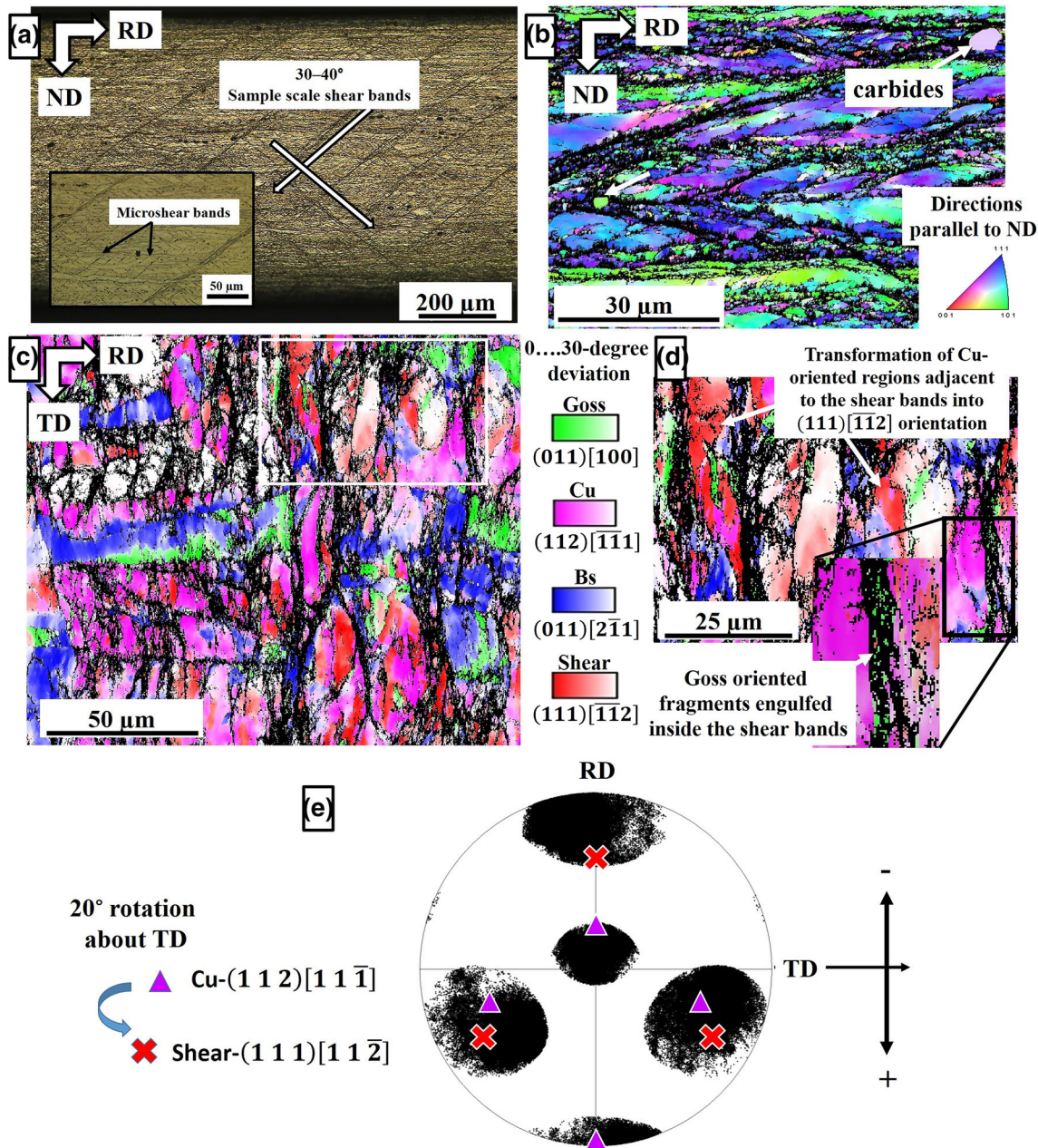


Fig. 7—Microstructure & microtextural features of the sample rolled to 90 pct reduction. (a) Optical micrographs showing intense shear banding at both micro and macroscales. (b) The IPF map taken from the RD-ND plane indicates the large-scale division of grains due to SBs. (c) Orientation image obtained from rolling plane (here, both microstructure and orientation image correspond to the RD-TD plane). (d) Enlarged view of the region marked in (c). (e) (111) Pole figure representing the positive rotation of Cu-(112)[111] oriented grains along TD toward shear-(111)[112] orientation (pole figure was obtained after partitioning out the Cu and shear orientation with 30 deg deviations from the total orientation data).

Grain misorientation distributions computed from orientation micrographs of different rolled samples are indicated in Figure 8. There is some deviation between correlated and uncorrelated misorientation distributions for the 30 pct rolled sample. Thereafter the deviation strongly builds up as rolling reduction increases. At 90 pct reduction, a substantial difference is observed between the two misorientation distributions discerned by a sharp rise in fraction of grains with lower correlated misorientation angles. This significant deviation cannot be simply associated with the Sachs mode of

crystallographic slip in the present study, as microstructural investigations have indicated the presence of large-scale shear banding after intermediate rolling stages. As shear banding is associated with non-crystallographic deformation, it does not inherently contribute to lattice rotations or GND evolutions. Instead, the deviation in grain misorientation distributions could be attributed to grain fragmentation that occurred by intensive shear banding [Figure 8(d)], which usually produces lower correlated misorientation angles [marked in Figure 8(c)] as most of the time the

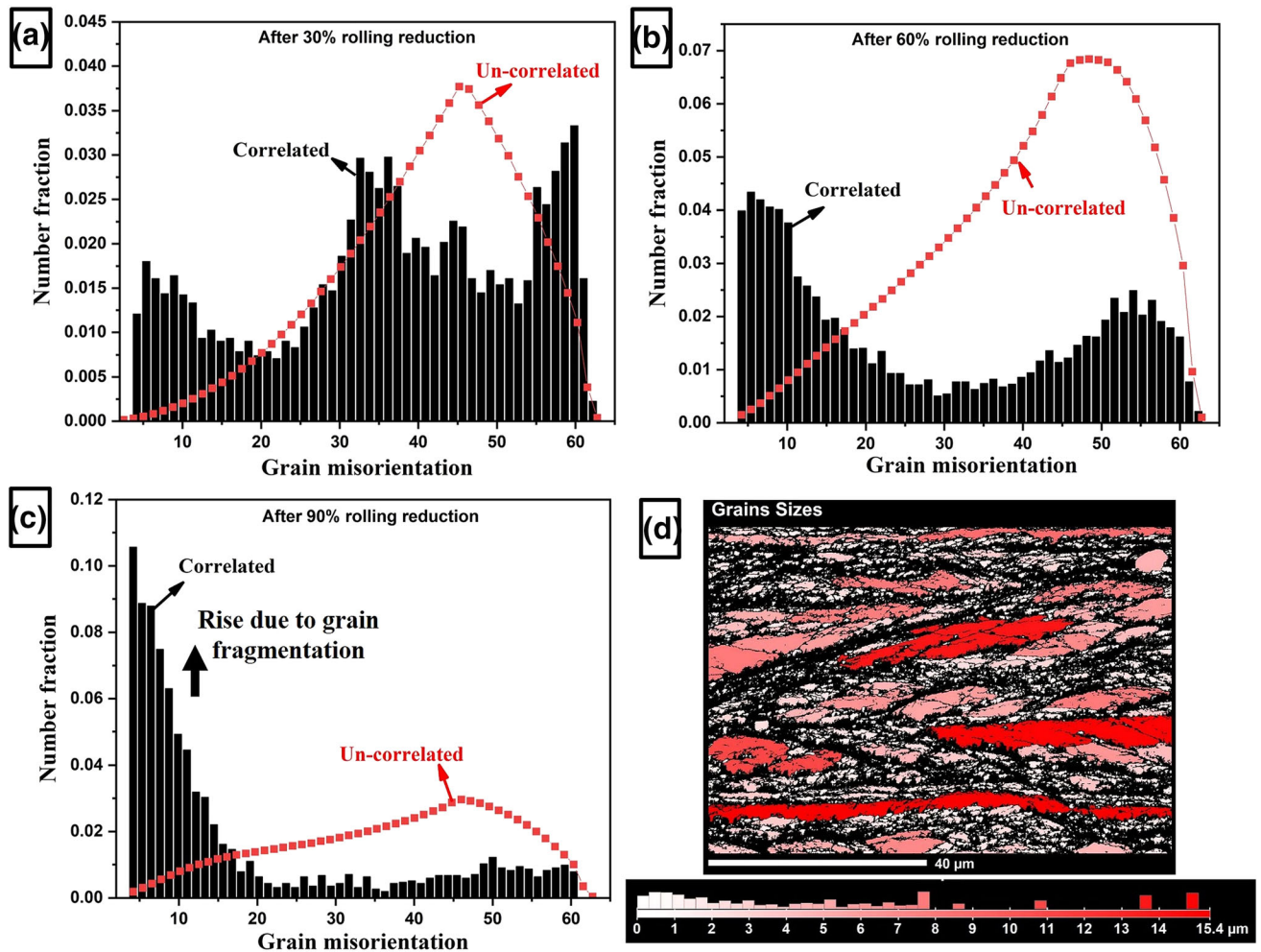


Fig. 8—Variation in the correlated and uncorrelated grain misorientation distributions as a function of percentage rolling reduction, (a) 30 pct, (b) 60 pct, and (c) 90 pct. (d) The grain size distribution of the 90 pct rolled sample indicating large-scale grain fragmentation due to intense shear banding.

neighboring grain fragments belong to same parent grain.

### E. Simulation of Experimental Texture Using VPSC

As mentioned in the previous section, discrepancy between correlated and uncorrelated misorientation distributions from early stages of rolling contemplates that deformation in alloy 625 is intermediate to the upper-bound Taylor's and lower bound Sach's models. Accordingly, the usage of  $n^{\text{eff}}$  scheme would be more appropriate. However, both  $n^{\text{eff}}$  and tangent schemes are adopted in the present study to model the experimental texture. Moreover, the effectiveness of simulation is identified by computing the error between simulated and experimental ODFs. The L1 loss function given by the following equation is utilized to compute the error:

$$\text{L1 loss function} = \sum |f(\mathbf{g})_{\text{exp}} - f(\mathbf{g})_{\text{sim}}| \quad [1]$$

In conjunction with the interaction scheme, the neighboring grain interactions have a decisive role in setting up different reorientation paths within a grain, leading to texture weakening. To account for these effects, in the present study, the reorientation of each grain has been coupled with the reorientation of a single random neighbor (*i.e.*, NEIGH = 1 in the VPSC input file). This ensures different rotation paths of grains with the same initial orientation due to a different neighbor, which ultimately slows down the texture evolution. The imposed plane strain velocity gradient matrix and the single crystal Voce hardening parameters are listed in Table II (see Figure 1 in Section II-C for more information on parameters). The initial texture for simulations is obtained by discretizing the base material's ODF into 5000 independent orientations. In the initial set of simulations, only octahedral slip ( $\{111\} \langle 110 \rangle$ ) is considered, as there is no observation of deformation twinning from microstructural investigations. Moreover, only isotropic hardening is considered for all the slip systems inside the grain, *i.e.*, latent hardening of secondary slip systems due to the active

**Table II. Single Crystal Voce Hardening Parameters of Slip and Partial Slip Systems Employed in the Present Study (See Fig. 1)**

	$\tau_0$	$\tau_1$	$\theta_0$	$\theta_1$
Slip $\{111\} \langle 110 \rangle$	80	135	390	115 (all are in MPa)
Partial Slip $\{111\} \langle 112 \rangle$	100	135	390	115
Imposed Velocity Gradient =	$\begin{bmatrix} 1 & 0 & 0 \\ 0 & 0 & 0 \\ 0 & 0 & -1 \end{bmatrix}$			

**Table III. Error Between the Experimental and Simulated ODFs Computed Using the L1 Loss Function Indicated in Equation [1]**

S.No.	Simulation Parameters	Rolling Reduction		
		30 pct ( $\epsilon = -0.36$ )	60 pct ( $\epsilon = -0.92$ )	90 pct ( $\epsilon = -2.3$ )
1.	$n^{\text{eff}}$ scheme ( $\mathbf{n} = 10$ ) only octahedral slip $\{111\}[110]$	0.068	0.19	0.387*
2.	tangent scheme ( $\mathbf{n} = 20$ ) only octahedral slip	0.074	0.194	0.39*
3.	$n^{\text{eff}}$ scheme octahedral slip $\{111\} \langle 110 \rangle$ + partial slip on $\{111\} \langle 112 \rangle$	0.105	0.28*	0.52*

\*The simulated texture deviates both quantitatively and qualitatively from the experimental texture.

slip system is not considered. As expected, the  $n^{\text{eff}}$  scheme was slightly more accurate in tracking experimental texture evolution in alloy 625 than the tangent scheme; the corresponding error is listed in Table III. However, simulated texture obtained from either scheme would only be able to track the experimental texture up to 60 pct reduction. At 90 pct reduction, simulated texture deviates qualitatively and quantitatively from the corresponding experimental texture as texture evolution nearly stagnates after the onset of large-scale shear banding (Figure 3). ODF sections of simulated texture obtained from running the  $n^{\text{eff}}$  scheme up to desired rolling reductions are indicated in Figures 9(a) through (c).

Incorporation of deformation heterogeneities like stacking faults or deformation twins (shear on  $\{111\} \langle 112 \rangle$ ) as the second deformation mode alongside octahedral slip in VPSC was considerable in tracking the Cu to Goss/Brass transition.<sup>[7,9]</sup> However, in the present study, incorporating partial or twin shear has shown texture deviating from experimental results from the initial rolling stages. ODF sections at 90 pct reduction obtained by including partial slip are indicated in Figure 9(d), and the corresponding error at various reductions is listed in Table III. As SBs form due to non-crystallographic slip of dislocations, they are yet to be modeled and incorporated in the VPSC code. Some studies<sup>[32,33]</sup> have developed modified constitutive equations that consider shear banding and fed them into crystal plasticity-based finite element modeling. It was successful in tracking stress-strain response and corresponding textural changes. However, this method is time-consuming and requires much computational energy and hence was not considered in the present study. On the other hand, a simple description can be adopted for the alloy 625 to qualitatively predict

evolution of  $\gamma$ -fiber at 90 pct reduction, which is addressed in the Section IV.

## IV. DISCUSSION

### A. Deformation Mechanisms: Low to Intermediate Levels of Rolling

Deformation in initial stages of rolling in alloy 625 occurred predominantly by dislocation slip ( $\{111\} \langle 110 \rangle$ ) as there are no indications of microstructural features pertaining to other deformation modes after 30 pct rolling [Figure 3(a)]. The corresponding development of Cu-type texture reconfirms dominance of octahedral slip-mediated deformation.<sup>[34]</sup> The microstructure also revealed existence of large misorientation deviations inside the grains, which are captured from the GROD map [Figure 4(b)]. Intra-grain misorientations associated with GNBs are usually developed during deformation to maintain microscopic strain compatibility between neighboring grains.<sup>[27,35]</sup> In general, neighboring grain interactions generate strain heterogeneities by disrupting uniform lattice rotation of the grain, primarily near boundary regions. Strain heterogeneities then impose local variation in dislocation slip activity from grain boundaries to the interior, resulting in various reorientation paths across the grain. However, with increase in deformation, a simultaneous crystallographic texture sharpening is expected as more grains/regions of grains with unstable orientations are transformed into relatively stable orientations.<sup>[9]</sup>

As rolling reduction reaches an intermediate level of 60 pct, it is evident from ODF plots [Figure 3(b)] that the alloy attains a characteristic Cu-type texture with a moderate rise in textural intensity ( $f(g)_{\text{max}} = 3.3$  m.r.d.). The sluggish texture strengthening observed

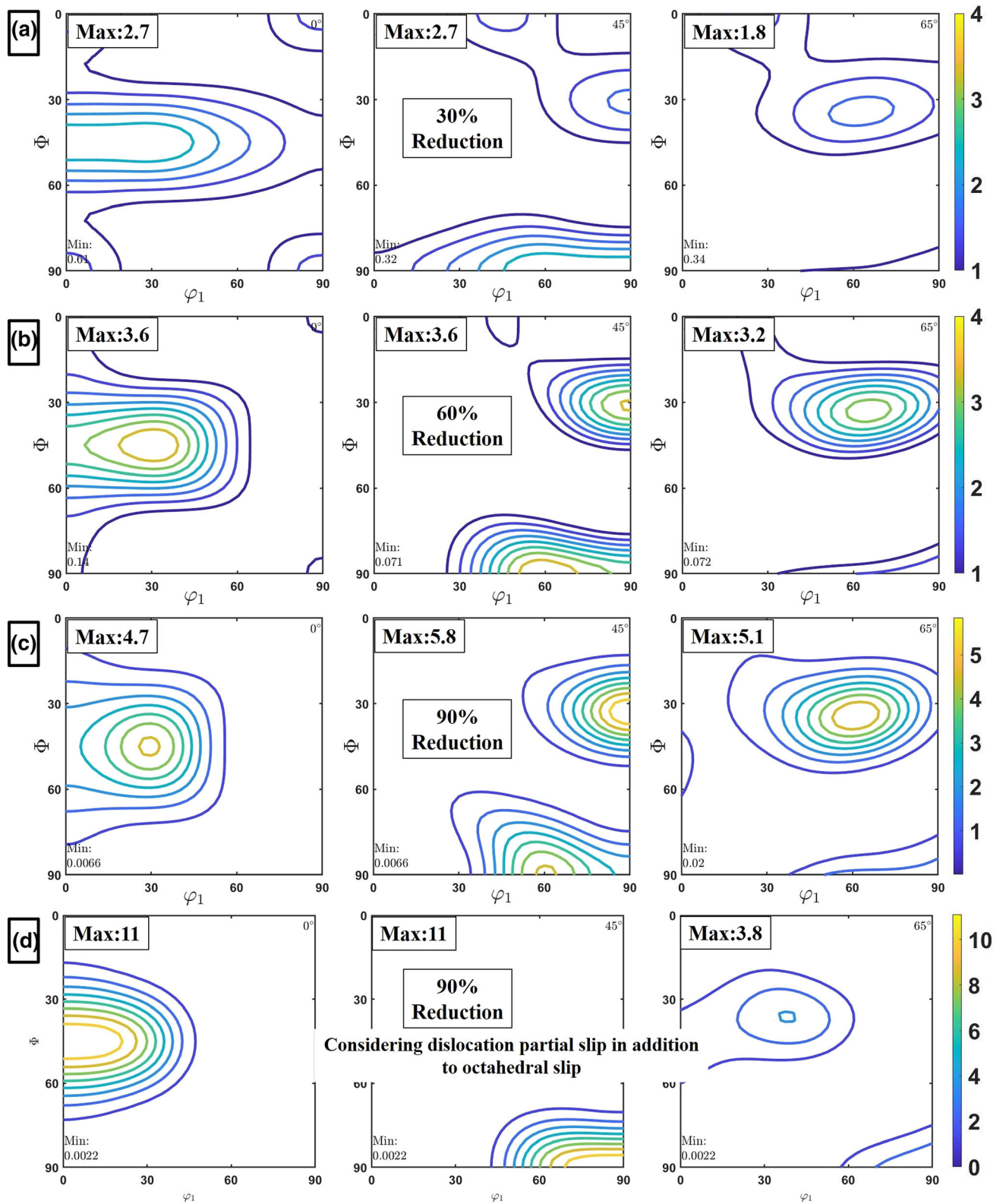


Fig. 9—(a) through (c) ODF sections  $\phi_2 = 0^\circ, 45^\circ$  and  $65^\circ$  of the simulated texture obtained by employing  $n^{\text{eff}}$  scheme with only octahedral slip activation for 30, 60, and 90 pct reduction, respectively. (d) The  $n^{\text{eff}}$  simulated texture obtained at 90 pct reduction by considering dislocation partial slip as a second deformation mode.

could be correlated to synergetic effect of severe work-hardening and neighboring grain interactions. Alloy 625 possesses a higher work-hardening rate as it is a concentrated solid solution alloy with a wider misfit in atomic radius of solute (Nb, Mo, and Cr) and matrix Ni atoms.<sup>[36]</sup> It is to be noted that although the substantial amount of solute in alloy 625 lowers SFE, it is the nature of solute atoms that have imparted even more strong dislocation—solute interactions, thereby further hindering dynamic recovery processes. This accounts for the simultaneous rise in self & latent hardening of active slip systems during deformation, ultimately retarding lattice rotations & weakening the entire texture. Besides textural implications, the corresponding effects of solute strengthening in alloy 625 could also be inferred from microstructural features that evolved up to this intermediate rolling stage.

The optical & orientation micrographs taken from the RD-ND plane of the sample rolled to 60 pct (Figure 6)

revealed traces of micro-SBs in some of the grains alongside the increased fraction of GNBs and associated grain fragmentation throughout the microstructure. Generally, it is believed that heterogeneous dislocation structures that precede shear banding play a crucial role in their nucleation. In this regard, the STEM micrographs (Figure 10) collected from the RD-ND plane of 60 pct rolled sample are utilized to understand the origin of shear banding in alloy 625. From these micrographs, it is apparent that the grains develop intense planar dislocation walls/ microbands with diffuse dislocation networks in the background. The microbands are usually formed by slip clustering on one of the  $\{111\}$  slip planes to accommodate small misorientation ( $\sim 2$  deg) changes between adjacent regions.<sup>[18]</sup> The lamellar structure of microbands is comparable to microtwin stacks that develop in low-SFE materials but the presence of the latter is discarded in the present study as no twin-related extra diffraction spots were

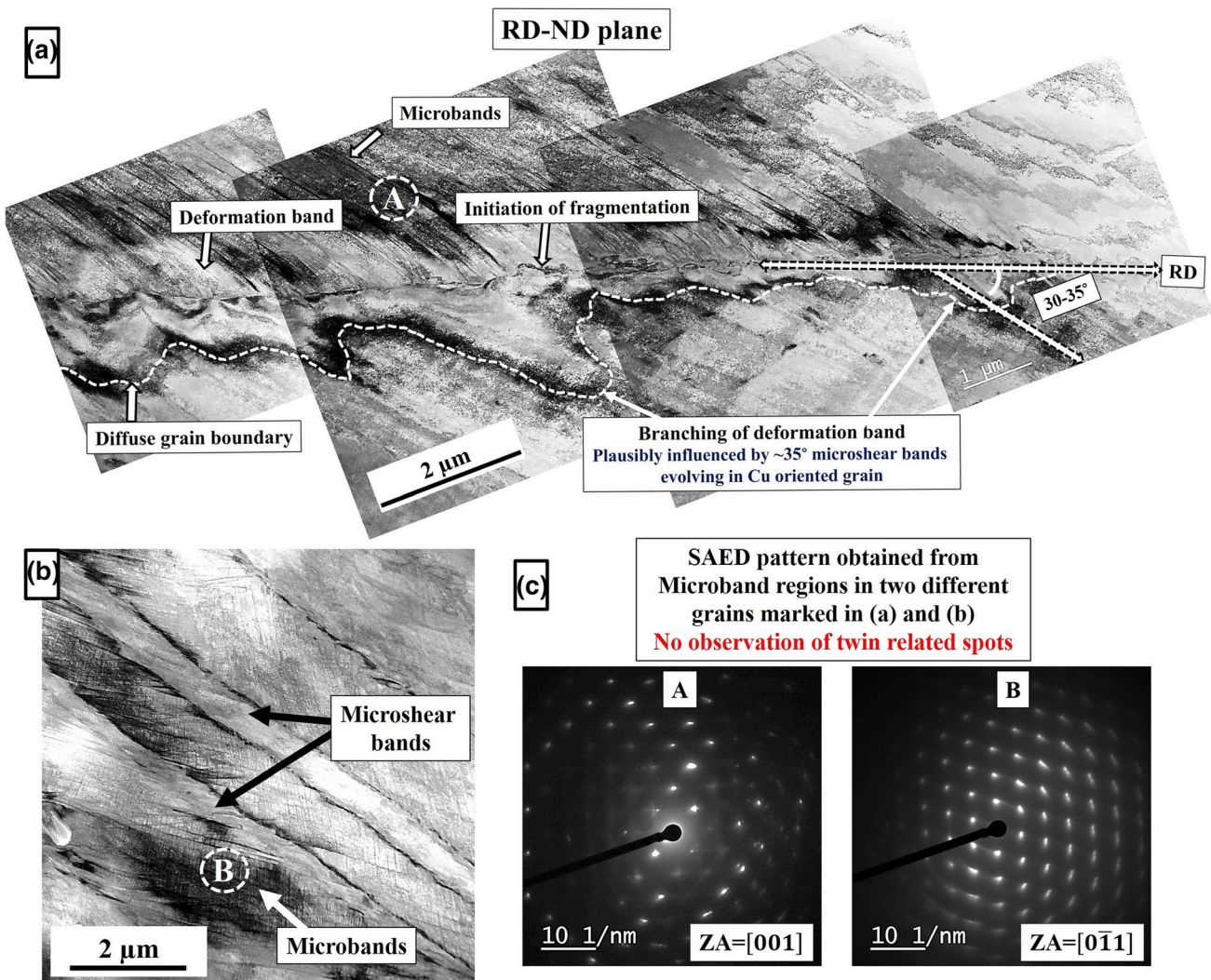


Fig. 10—STEM micrographs obtained from the RD-ND plane of sample rolled to 60 pct reduction (a) Stretched micrograph representing intense microbanding within the grains along with the deformation band at the diffused boundary; this whole region is similar to that shown in Fig. 6(d). (b) Micrograph of one of the grains, where micro-SBs are activated and found cutting through the intensive microbanded regions. (c) SAED patterns acquired from the microband regions marked in (a) and (b).

observed in corresponding SAED patterns [Figure 10(c)]. Therefore, microbanding could solely be held responsible for inhibition of dislocation mobility and further activation of SBs in alloy 625. It has also been reported that during rolling of single crystals, microbands could act as precursors for nucleation of SBs.<sup>[37]</sup> Overall, it could be said that the rolling deformation sequence observed in alloy 625 under warm conditions is planar dislocation slip → microbanding → shear banding.

Several researchers<sup>[25,30,33]</sup> who performed single crystal rolling experiments have suggested that the tendency of microbanding and subsequent shear band formation is a function of crystal orientation besides the material properties. Unlike single crystal rolling, there are limited studies on polycrystalline materials where additional effects of neighbors on reorientation path of individual grains and associated heterogeneities are considered. In this regard, a crystal orientation map [Figure 6(c)] plotted from EBSD data of 60 pct rolled sample is utilized to demarcate the major rolling components whose deformation characteristics are addressed separately in the following subsections.

#### 1. Goss $\{110\} \langle 001 \rangle$ & Bs $\{110\} \langle 112 \rangle$ Orientations

The Goss single crystal under plane strain compression (PSC) generally deforms by uniform slip distribution on the four active slip planes (Table IV) and is stable up to a significant thickness reduction. However, it has been reported that at higher deformation strains, the Goss crystal splits along  $\alpha$ -fiber into complementary Bs orientations by undergoing rotations about ND.<sup>[38,39]</sup> In an attempt to describe the ND rotations, Becker<sup>[40]</sup> has shown that restricting RD-TD shear component ( $\epsilon_{RD-TD}$ ) would make Goss crystal unstable and promote orientation gradient along  $\alpha$ -fiber. In comparison to single crystals, deformation of Goss-oriented grains in a polycrystalline material is difficult to assess, as initial deviation of the grain from ideal Goss position and neighboring grain interactions have a strong influence. Nevertheless, some degree of interpretation can be made between lattice rotations in Goss-oriented grain with orientation of the neighboring grains.

The orientation micrograph of 60 pct rolled sample [Figures 6(c) and (d)] represents that the Goss appears in microstructure as two distinctive features, (a) as a grain, which is initially oriented/reoriented during deformation and (b) as a deformation band (DB) region near the boundaries of grain that has been reoriented toward Bs. In order to describe the neighboring grain interactions, three different Goss regions surrounded by Bs and Cu-oriented grains are selected and their enlarged views with corresponding (111) pole figures plotted onto the RD-TD plane are depicted in Figure 11. The primary observation is that part of the Goss regions undergoes lattice rotations around ND, which are similar but only occur at a significant strain in case of single crystal rolling experiments. The key observations made from these micrographs are listed below

- (a) When the Goss-oriented region (as grain) contains Bs on one side and Cu on the other, the lattice rotations around ND are seen to be confined near the grain boundaries that are shared with the Bs-oriented grain [Figure 11(a)].
- (b) The Goss-oriented region (as grain) surrounded by Cu on both sides has undergone grain splitting by producing two complementary Bs orientations [Figure 11(b)].
- (c) The Goss-oriented regions (as DBs) observed near the boundaries of Bs-oriented grains are also seen to undergo lattice rotations around ND toward Bs [Figure 11(c)].
- (d) Alongside significant ND rotations, some TD rotations are also developed in the Goss regions.

In general, only two slip systems are activated in Bs grains under PSC and uniform slip on them produces a grain scale  $\epsilon_{RD-TD}$  shear component (Table IV).<sup>[25]</sup> It has been observed that the Bs grains during rolling deformation enforce this  $\epsilon_{RD-TD}$  shear onto the neighboring grains probably as Bs orientation is a hard and energetically favorable orientation on  $\alpha$ -fiber in low-to-medium-SFE materials.<sup>[40,41]</sup> In such a scenario, the neighboring Goss-oriented grains which experience the RD-TD shear would try to restrict it and thereby develop reaction stresses that mediate Goss regions near the grain boundaries to undergo ND rotations toward Bs. Nevertheless, the rotation path set toward Bs stays incomplete in most cases due to the formation of GNBs and associated grain fragmentation. This could be a possible reason for the observed rise in intensity of orientations spread between Goss and Bs positions along  $\alpha$ -fiber as rolling reduction increases (Figure 3). In another instance, where Goss grain is surrounded by Cu grains on both sides, grain splitting into complementary Bs orientations is seen. Here, rotations around ND are not just limited to grain boundaries but are extended into the grain interiors. Therefore, as described by Becker,<sup>[40]</sup> the varying degree of constraints arising from interior to the boundaries of Goss-oriented grains (most notably, RD-TD shear) would always promote lattice rotations along ND toward stable Bs orientation.

In contrast to the Goss orientation, the Bs-oriented grains are less susceptible to lattice rotations.<sup>[25]</sup> However, in the present study, it is noticed that in most of the cases, the Bs grains besides the Cu neighbors were influenced to develop Goss-oriented DBs in some parts of the grain boundary regions (Figure 6). It should be noted that Cu is a relatively hard orientation compared to Bs under PSC due to the higher value of Taylor factor ( $M$ ) (Table IV). Therefore, reaction stresses generated at interfaces of Cu & Bs-oriented grains are forced back onto the Bs side, leading to activation of a different set of slip systems near grain boundary regions of Bs grains. It can be contemplated that this new set of slip systems is responsible for the evolution of Goss-oriented DBs. Moreover, preference for a Goss-oriented neighbor by

**Table IV. The Active Slip Systems in Goss, Bs and Cu Single Crystals Under Taylor's Fully Constrained Plane Strain Condition (FC PSC) and the Corresponding Development of Macroscopic Shear Component per Unit Slip on Activated Slip Systems<sup>[25]</sup>**

Orientation	Active Slip Systems Under FC PSC Condition (At a Given Taylor Factor) Orientation, All Slip Systems have Equal Schmid Factors	Taylor Factor $M = \sum_s \frac{\dot{\gamma}_s}{\dot{\epsilon}}$	Sample Scale Shear Components Generated per Unit Imposed Strain $\epsilon$		
			$\epsilon_{RD-TD}$	$\epsilon_{ND-RD}$	$\epsilon_{TD-ND}$
Goss	$\{111\}\langle 01\bar{1}\rangle, \{111\}\langle \bar{1}01\rangle, \{\bar{1}\bar{1}1\}\langle 0\bar{1}\bar{1}\rangle, \{\bar{1}\bar{1}1\}\langle 0\bar{1}\bar{1}\rangle$	2.45	0	0	0
Brass (Bs)	$\{111\}\langle \bar{1}\bar{1}0\rangle, \{\bar{1}\bar{1}1\}\langle 101\rangle$	2.45	- 0.289*	0	0
Copper (Cu)	$\{111\}\langle 01\bar{1}\rangle, \{111\}\langle \bar{1}01\rangle, \{\bar{1}\bar{1}1\}\langle \bar{1}\bar{1}0\rangle, \{\bar{1}\bar{1}1\}\langle \bar{1}\bar{1}0\rangle$	3.67	0	- 0.481*	0

\*The generation of the shear components makes Bs and Cu unstable under FC PSC mode.

both Cu and Bs grains implies that Goss is a soft orientation that consumes the stresses generated from neighbors and undergoes local lattice rotations with minimum geometrical strain hardening.

## 2. Cu $\{112\} \langle 111 \rangle$ Orientation

The orientation micrograph of 60 pct rolled sample of alloy 625 indicated occurrence of micro-SBs in some of the Cu-oriented grains. An enlarged view of one of the grains with SBs is shown in Figure 12(a). Numerous studies<sup>[25,30,33,37]</sup> on rolling deformation behavior of FCC single crystals have concluded that the Cu orientation has a higher tendency of shear band formation than others. This behavior has been interconnected to uneven slip distribution on active slip system pairs due to their asymmetrical inclinations to the RD. Geometry of slip systems in Cu crystal under PSC condition is shown in Figure 12(b). As described in the schematic, the Cu-oriented crystal deforms by producing shear on coplanar (CP: slip on  $\{111\}$  plane in  $\langle 01\bar{1}\rangle$  and  $\langle \bar{1}01\rangle$  directions) and co-directional (CD: slip on  $\{\bar{1}\bar{1}1\}$  and  $\{\bar{1}\bar{1}1\}$  planes in  $\langle \bar{1}\bar{1}0\rangle$  direction) slip system pairs with an equivalent Schmid factor.<sup>[25]</sup> However, due to asymmetry, the shear on the CP pair is twice that of the CD pair leading to the early formation of inhomogeneous dislocation structures. Further, successive activity of these slip system pairs during deformation would stabilize Cu orientation, but only at the expense of producing a macroscopic  $\epsilon_{ND-RD}$  shear component (Table IV). Wagner *et al.*,<sup>[30]</sup> in their study on rolling deformation of Cu-oriented single crystals, have suggested that restriction of  $\epsilon_{ND-RD}$  component at initial stages of rolling deformation (following FC condition) would preferentially promote dislocation slip on CD pair resulting in + TD lattice rotation toward Dillamore orientation  $\{4411\}\langle 11118\rangle$ . However, for Dillamore orientation, the Schmid factor for CP pair becomes greater than that of CD, thereby redirecting most dislocation slip back onto the CP pair. This slip transfer from CD to CP pair would then produce - TD rotations and set up a reorientation path back toward the original Cu orientation. At this deformation stage, Wagner *et al.* hypothesized that the material with a lower propensity of dislocation cross-slip develops microbands on the CP due to dominant slip activity. Further, it is understood that microbands would latent

harden the CD pair and ultimately raise the local stresses to a state where nucleation of SBs occurs.

STEM micrograph taken from RD-ND plane of the 60 pct rolled sample [Figure 12(c)] gives microstructural evidence of microbanding on the CP slip plane alongside micro-SBs that run through them. Further, it may be noticed that the micro-SBs exist as colonies of fine bands separated with intermediate matrix regions, where dislocation activity is also seen on a new slip system different from CP and CD pairs (depicted in schematic adjoining the STEM micrograph). Generally, it is believed that compatibility issues raised at grain boundaries by large positive shear in the bands could be relaxed to some extent by producing a negative shear in these intermediate regions.<sup>[30]</sup> Therefore, stacks of finer bands with intermediate regions constitute a microshear band. Microstructure development inside SBs captured in TEM [Figure 12(d)] indicates an avalanche of dislocation slip within the bands, constituting a heavily distorted medium along with some less distorted regions entrapped in it. The SAED pattern collected from these less distorted regions shows a different zone axis compared to matrix regions adjacent to the SBs, suggesting that these regions underwent large-scale lattice rotations either through dislocation slip or by rigid body rotations.<sup>[30]</sup> Moreover, these regions are distributed randomly inside the SBs.

The (111) pole figures of Cu-oriented grains with and without SBs [Figures 12(e) and (f)] show that the lattice rotation path from Cu to Dillamore reported by Wagner *et al.*<sup>[30]</sup> was also followed by Cu-oriented grains in the studied polycrystalline alloy 625. The only new observation is that in addition to TD rotations, the ND rotations were also prevalent due to neighboring grain interactions from Goss and Bs-oriented grains. Moreover, corresponding orientation micrograph of the shear banded Cu grain shown in Figure 12(a) also depicts that the part of Cu matrix region on the side of SBs is transforming toward Bs orientation, which usually takes place in low-to-medium-SFE materials. However, lattice rotation rates are so weak in alloy 625 that they only lead to orientations intermediate to the Cu and Bs, represented by large intensity spread in the corresponding (111) pole figure [Figure 12(f)]. In regard to orientations that form inside the bands, it was reported that regions within the bands undergo large-scale

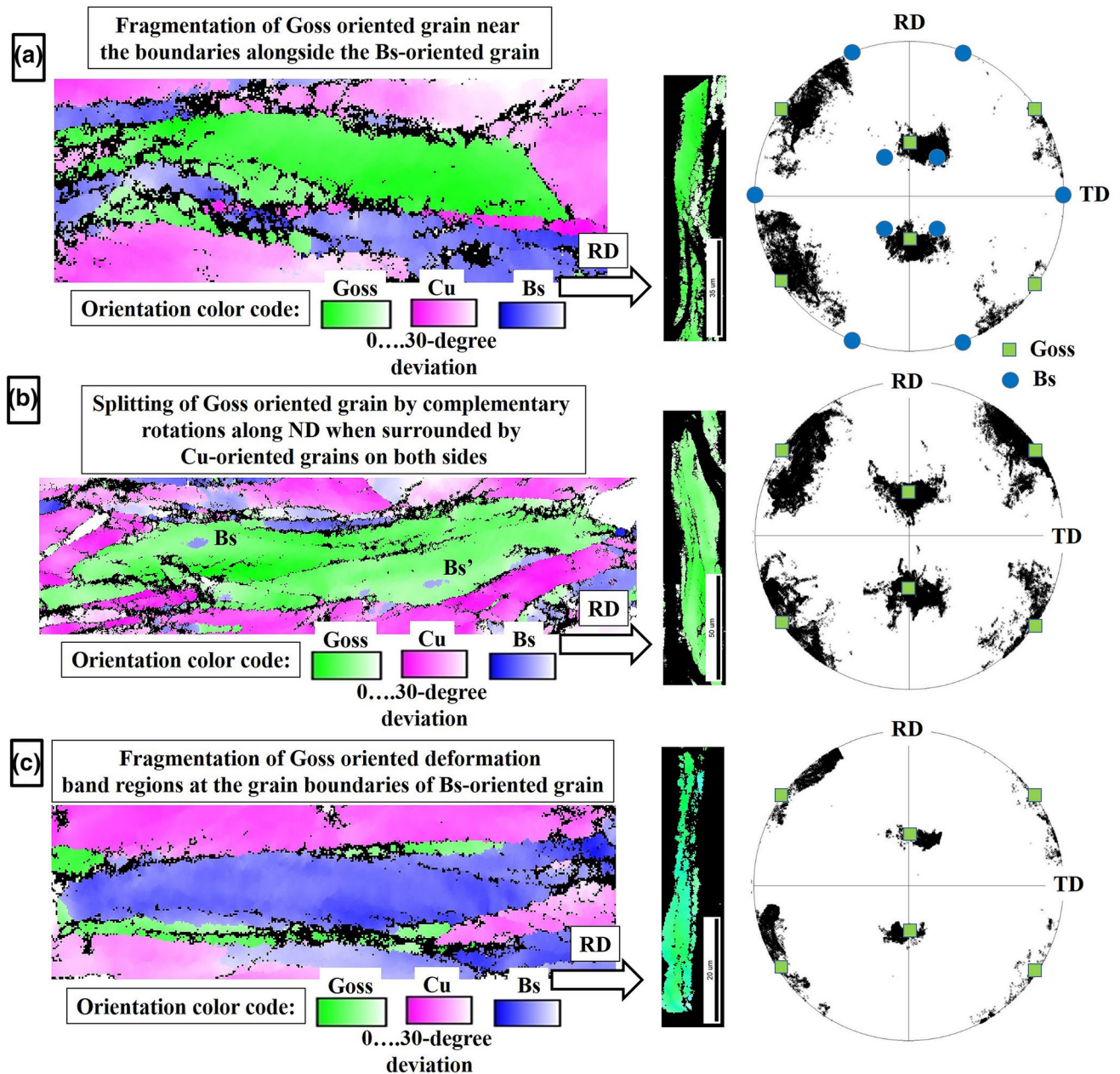


Fig. 11—Deformation characteristics of Goss-oriented grains/DBs surrounded by different neighbors. Orientation micrographs and corresponding (111) pole figures of (a) Goss-oriented grain surrounded by Cu on one side and Bs on the other, (b) Goss-oriented grain surrounded by Cu on both sides, (c) Goss-oriented DBs emerged at the grain boundary of Bs-oriented grain. All Goss-oriented grains/DBs undergo lattice rotations around ND ( $\sim 25$  deg). In most cases, the lattice rotations are seen to be restricted to the boundary regions on the side of Bs neighbor, promoting grain fragmentation. Without Bs neighbor, the lattice rotations spread into the grain.

positive and negative rotations around TD to achieve Goss ( $-55$  deg TD rotation) or Cube ( $+35$  deg TD rotation) orientations.<sup>[25,30]</sup> However, in the present study, orientation changes occurring inside the bands are not adequately captured from orientation micrographs as they are mostly non-indexed due to a largely distorted area. Although a few indexed regions with Goss orientation are seen within the bands, which may correspond to the less distorted regions as mentioned earlier from TEM micrographs.

In the present study, SBs formed in Cu-oriented grains are nearly inclined at  $\pm 35$  deg to the RD, which is a common observation in cold-rolled FCC materials. Generally, SBs evolve on principal shear stress planes that are inclined at 45 deg to loading axis, for example, shear band formation due to localized adiabatic heating during hot deformation. The reason behind deviation from 45 deg and the specific inclination near 35 deg observed in cold-rolled materials was first established by Dillamore *et al.*<sup>[29]</sup> They proposed that SBs generate



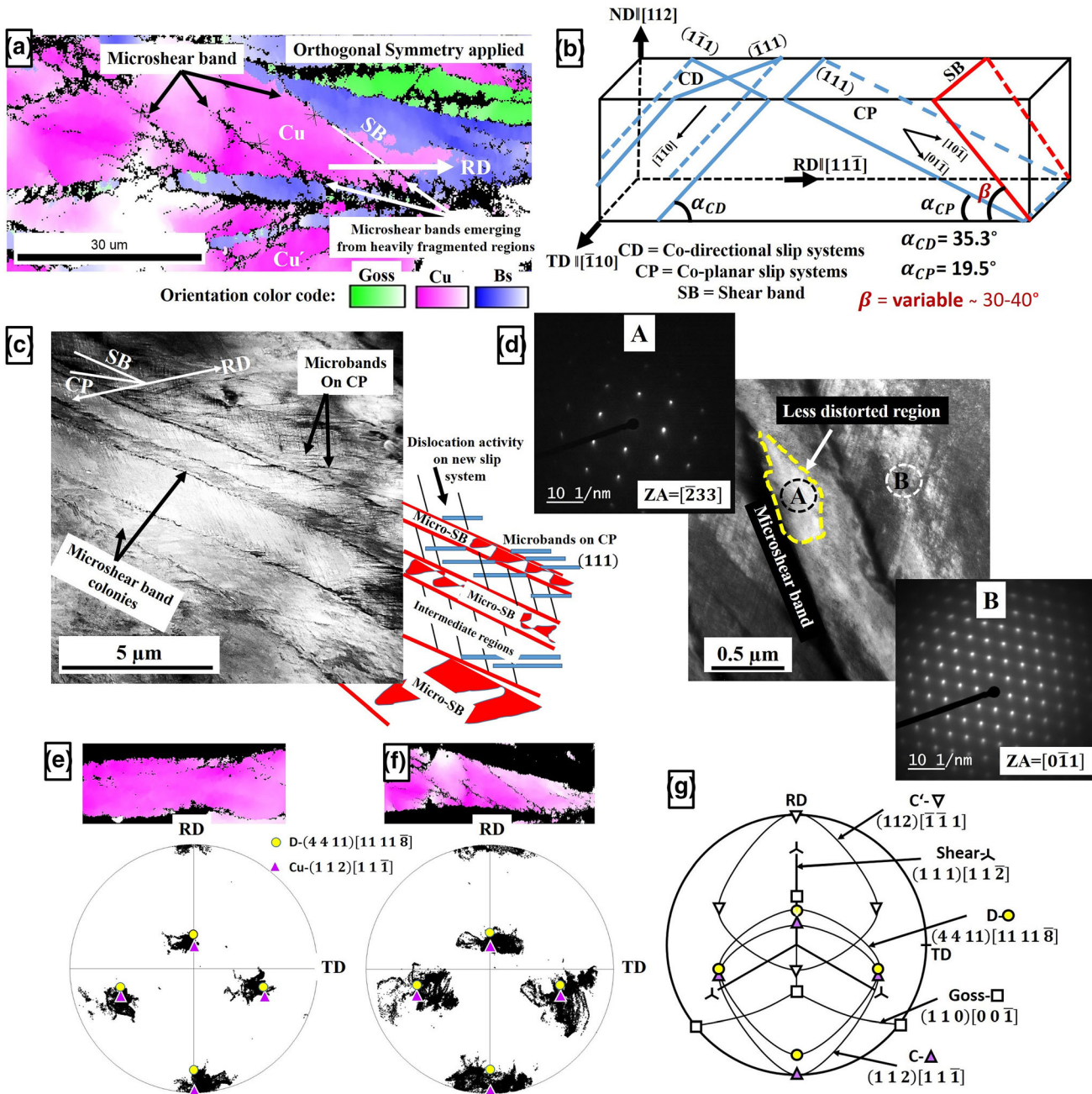


Fig. 12—Deformation characteristics of Cu-oriented grain. (a) Orientation image representing the emergence of micro-SBs in Cu-oriented grain from the fragmented boundary region (here, orientations are projected onto the RD-TD plane while microstructure still represents the RD-ND plane). (b) Schematic of the active slip systems in Cu-oriented crystal under FC plane strain condition.<sup>[25,30]</sup> (c, d) STEM and TEM micrographs of the microshear band colonies in one of the grains (taken from RD-ND plane), tentative rolling direction assumed from slip and shear band geometry is indicated. (e) and (f) Comparison of (111) pole figures of non-shear banded and shear banded grain, (g) Stereographic projection of 111 poles on to RD-TD plane indicate the position of different orientation components generated by  $\pm$  TD rotations of Cu-oriented crystal<sup>[30]</sup>.

inside the grains of textured polycrystalline aggregate as a consequence of geometrical softening (negative  $dM/d\varepsilon$ ) arising from plastic anisotropy. The instability condition for shear banding for a particular grain could be derived from Taylor's strain hardening equation.

$$\sigma = M\tau_s \quad [2]$$

where  $\sigma$  is the macroscopic stress,  $M$  is the Taylor factor, and  $\tau_s$  is the microscopic shear stress on active slip systems. Differentiation of equation [2] gives

$$\frac{d\sigma}{d\varepsilon} = \frac{dM}{d\varepsilon} \tau_s + M \frac{d\tau_s}{d\varepsilon} = \frac{dM}{d\varepsilon} \tau_s + M^2 \frac{d\tau_s}{d\gamma} \left( M = \frac{d\gamma}{d\varepsilon} \right) \quad [3]$$

The above equation explains that when the strain hardening rate,  $\frac{d\sigma_s}{d\epsilon}$  tends to 0, plastic instability through shear banding occurs in those grains in which  $\frac{dM}{d\epsilon}$  attains negative values earliest. This approach also predicts the tendency of Cu-oriented grains to develop SBs at intermediate level of deformation compared to the others. This can be confirmed by considering the following points

- (a) Cu orientation exhibits a comparatively large  $M$  of 3.65 (Table IV). This indicates that it requires more plastic work on individual slip systems per unit amount of external strain, suggesting that dislocation–dislocation interactions are more prominent in Cu-oriented grains and result in a higher strain hardening rate at the initial stages of deformation followed by early saturation.
- (b) Taylor factor calculations for orientations lying on  $\beta$ -fiber have shown that  $M$  is largest for Cu orientation and drops drastically as one moves away from this orientation toward Cube or Goss.<sup>[25]</sup> Therefore,  $\frac{dM}{d\epsilon}$  attains negative values faster for Cu orientation due to  $\pm$  TD rotations during deformation.

Moreover, it should be noted that a direct correlation of geometrical softening mechanism for formation of a shear band cannot be applied when there are neighboring grain interactions, as the  $M$  value varies from grain boundaries to grain interior due to the formation of GNBs. However, Cu being a hard orientation, it sustained less degree of orientation spread compared to others giving the scope for geometric softening. Furthermore, SBs in the present alloy are seen to be emerging from heavily strained grain boundary regions or those regions where grain fragmentation has taken place [Figure 12(a)]. Therefore, local stress variations caused due to irregular strain accommodations near grain boundaries would lead to stress concentrations, which inherently trigger the nucleation of SBs.

### B. Deformation Mechanisms: Intermediate to High Levels of Rolling

Deformation after intermediate stages of warm rolling was dominated by shear banding. An extensive banded structure is evident from micrographs of the 90 pct rolled sample (Figure 7). Both sets of positive and negative SBs have emerged and most of them are seen extended along the band direction becoming sample scale. Usually, in concentrated solid solution alloys, after initiation of micro-SBs in Cu-oriented grains, a certain amount of shearing takes place parallel to the bands until deformation on regular octahedral systems resurfaces with some restrictions.<sup>[11]</sup> Further, intermittent shear contributions from shear banding and non-intersecting slip systems would influence lattice rotations of Cu-oriented grains, ultimately accounting for Cu to Bs-type texture transition.<sup>[6,11]</sup> However, the near saturation of texture evolution observed in alloy 625 after 60 pct rolling reduction (Figure 3) indicates that dislocation mobility on active slip systems is mostly

getting exhausted and could not compete with mesoscopic shear occurring along the SBs. The peak generated at lower correlated grain misorientation angles for the 90 pct rolled sample [Figure 8(c)] further supports the above proposition of the occurrence of predominant non-crystallographic deformation. Heavy strain localization through shear banding resulted in grain fragmentation with fragmented regions undergoing limited lattice rotations [Figures 8(c) and (d)], leading to lower correlated grain misorientations.

Another crucial result of the present study is the apparent loss of intensity at Cu position with a parallel rise in the intensity spread over the  $\gamma$ -fiber ( $\langle\{111\}\parallel\text{ND}\rangle$ ) after 90 pct rolling [Figure 3(c)]. It was previously reported that the  $\gamma$ -fiber appeared as metastable orientations in low-SFE materials during rolling, and their existence was attributed to the progressive rigid body rotations of twin lamellae to align along the RD plane as a consequence of latent hardening effects in surrounding matrix.<sup>[8,42,43]</sup> In contrast, the present alloy 625 does not develop deformation twins at any rolling stage. In another study, Engler *et al.*<sup>[44]</sup> have demonstrated that rolled materials develop through-thickness texture gradient due to shear generated by small/extremely high roll draughts (*i.e.*, when the ratio of contact length to mean thickness is  $< 1$  or it is  $> 5$ ), which would ultimately produce rotated Cube ( $\{001\}\langle 110\rangle$ ) and  $\gamma$ -fiber components in addition to the standard FCC rolling texture components. Then, they modeled this phenomenon through VPSC by incorporating geometry and friction-induced shear into the variable plane strain velocity gradient matrix (deviating strain path from PSC). But, in the present study, firstly, the roll draught was maintained above 1 in all rolling steps [Figures 13(a) and (b)], and secondly, texture studies are only made at the mid-thickness level, where friction effects are the minimum. Therefore,  $\gamma$ -fiber development observed after 90 pct rolling for the present case cannot be simply correlated to rolling draught as described by Engler. Instead, reaction stresses generated along both positive and negative sets of sample scale SBs have played a significant role in texture transition as discussed in the following paragraph.

Due to extensive shear banding, positive SBs that reach sample scale would interact with roller contacts and build-up reaction stresses that eventually make them undergo rigid body rotations toward the compression plane [Figure 13(a)].<sup>[25,30]</sup> However, with the onset of negative SBs, rotations of positive SBs get obstructed. Further, to comply with microscopic boundary conditions, reaction stresses are transferred to complementary micro-SBs and ultimately to the rhomboidal prism regions enclosed between them. In this process, the corresponding regions become independent and would now be constricted to deform according to stresses enforced by the SBs. Furthermore, the geometry of reaction stresses across a rhomboidal region resembles a state of pure shear, where reaction stresses can be resolved along principal stress directions that act parallel and perpendicular to the compression plane [Figures 13(c) and (d)]. This stress state is characterized by material compression in ND direction and tension along

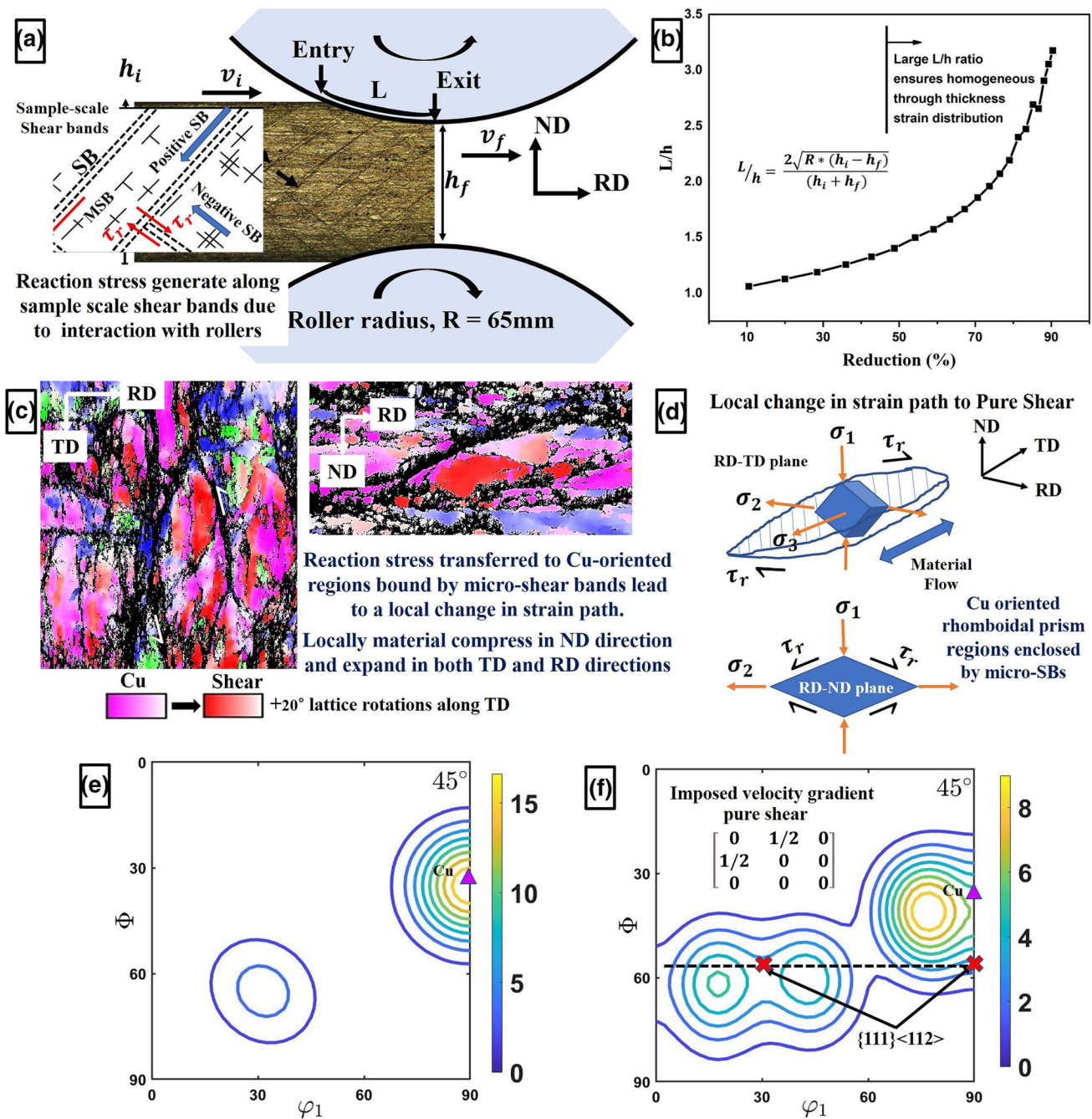


Fig. 13—(a) Roll gap geometry and schematic showing reaction stresses generated at the sample scale SBs due to interaction with the rolls, (b) Roll draught (ratio of contact length to mean thickness) computed for different steps of rolling in the present study, (c) Orientation micrographs taken from RD-TD and RD-ND sections indicating the transformation of Cu-oriented rhombohedral regions trapped in between the SBs to shear orientation, (d) Schematic indicating the change in strain path of entrapped rhombohedral regions from plane strain to pure shear resulting in homogeneous flattening by compression in ND and tension in both RD and TD directions. ODF section  $\phi_2 = 45^\circ$  of (e) unimodal Cu with a Gaussian width of 7.5 deg and (f) Simulated texture at  $\epsilon = -1.38$  obtained by imposing pure shear velocity gradient on unimodal Cu in the VPSC tool.

both TD and RD directions. Therefore, it could be reasonable to assume that regions enclosed by complementary SBs would undergo a local change in strain path from the bulk-imposed plane strain to the pure shear condition, that ultimately result in the homogeneous flattening of these regions. With combined effects of significant reaction stresses and subsequent change in

strain path, the enclosed regions would independently deform by dislocation slip on new octahedral slip systems, thereby imparting textural changes. Since Cu-oriented enclosed regions are predominant in the microstructure due to their tendency to form SBs as seen from orientation micrographs [Figure 13(c)], lattice rotations of this orientation under pure shear would

majorly contribute to the final texture. To comprehend the rotation path of independent Cu-oriented regions under pure shear, simulation using the VPSC model was performed. Texture representing unimodal Cu with a Gaussian width of 7.5 deg [Figure 13(e)] was fed as input to track textural changes when a pure shear strain velocity gradient is imposed. Simulation outcome through ODF  $\varphi_2 = 45$  deg section is shown in Figure 13(f). The simulated texture changes qualitatively resemble experimental texture intensity rise over  $\gamma$ -fiber observed in the present study and prove that Cu-oriented regions surrounded by SBs indeed undergo strain path change from plane strain to pure shear. It is to be noted that simulations are carried out without considering prior hardening and the subsequent latent hardening of new slip systems, hence no quantitative relation is seen between the experimental and simulated intensities. Quantitative texture predictions are targeted in our future studies.

## V. CONCLUSIONS

In the present work, the crystallographic texture evolution in alloy 625 during warm rolling and the underlying deformation micromechanisms were investigated. The experimental results are complemented by detailed microstructural examination and crystal plasticity simulations. The major findings are summarized as follows:

1. Alloy 625 develops a weak Cu-type texture up to intermediate rolling levels with planar dislocation slip as the dominant deformation mechanism. The development of weak texture is attributed to the sluggish lattice rotations caused by the higher work-hardening rate of the alloy.
2. Microband structures followed by planar dislocation slip is identified as the precursor for the nucleation of micro-SBs in the alloy 625. It is seen that micro-SBs are originated in Cu-oriented grains and further extended to the sample scale by crossing Bs grains. Accordingly, there is a loss in the texture intensity around both Cu and Bs positions. However, Goss grains were found to be more resistant to shear banding.
3. The higher propensity of shear banding in alloy 625 has led to the concurrent nucleation of new sets of complementary micro-SBs ( $\pm 30$  to  $40$  deg), which has subdivided the grains into rhomboidal fragments. Moreover, at large strains, the SBs undergo rigid body rotations toward compression plane due to the action of reaction stresses caused by roller contacts. This phenomenon influences further orientation changes of adjacent matrix regions.
4. Though alloy 625 is a concentrated solid solution alloy, Cu  $\rightarrow$  Bs -type texture transition mediated by synergetic activation of shear banding and non-intersecting slip systems is not observed in it. Instead, the deformation after intermediate stage of rolling ( $\sim 60$  pct) is predominantly carried forward by extensive shear banding, leading to overall texture

saturation. The drastic shift in the deformation mode is correlated to the large initial work-hardening rates and early exhaustion of active slip systems in the studied alloy.

5. A new intensity around  $\gamma$ -fiber  $\langle 111 \rangle \parallel \text{ND}$  texture observed after 90 pct rolling reduction in alloy 625 is attributed to a change in the strain path of fragmented grains (surrounded by complementary micro-SBs) from plane strain to pure shear. The strain path change is conceptualized based on the geometry of reaction stresses and further validated by performing VPSC simulation.

## ACKNOWLEDGMENTS

The authors acknowledge the funding by the Science and Engineering Research Board, Government of India, through Grant No. CRG/2019/000949 and the support of the material from MIDHANI LTD., Hyderabad, India. The authors are also thankful to the Metallurgical and Materials Engineering Department, IIT Roorkee, for permitting use of different experimental facilities.

## CONFLICT OF INTEREST

The authors declare no conflict of interest.

## APPENDIX

### Basic Formulation of the VPSC Model

The VPSC model considers the slip inside the grain to be rate dependent, and correspondingly, the strain rate ( $\dot{\epsilon}_{ij}$ ) and stress ( $\sigma$ ) states inside the grain are related by a viscoplastic constitutive law as follows:

$$\dot{\epsilon}_{ij} = \dot{\gamma}_0 \sum_s m_{ij}^s \left[ \frac{\tau_{\text{RSS}}^s}{\tau_{\text{CRSS}}^s} \right]^n = \dot{\gamma}_0 \sum_s m_{ij}^s \left[ \frac{m_{kl}^s \sigma_{kl}}{\tau_{\text{CRSS}}^s} \right]^n, \quad [\text{A1}]$$

where  $\dot{\gamma}_0$  is the reference strain rate corresponding to the initial critical resolved shear stress; exponent  $n$  is the inverse of strain rate sensitivity; suffix  $s$  refers to the slip system;  $m_{ij}^s$  is the symmetric part of Schmid tensor given by

$$m_{ij}^s = \frac{1}{2} (b_i^s n_j^s + b_j^s n_i^s) \quad [\text{A2}]$$

Here,  $b$  and  $n$  are burgers vector and slip normal of the system, respectively. In Eq. (A1),  $\tau_{\text{RSS}}^s = m_{kl}^s \sigma_{kl}$  is the resolved shear stress on the respective slip system, which evolves during the deformation. Slip on a given system takes place when resolved shear stress  $\tau_{\text{RSS}}^s$  on that system exceeds the critical shear stress  $\tau_{\text{CRSS}}^s$ . In addition, due to work hardening, the  $\tau_{\text{CRSS}}^s$  for dislocation slip to take place on a particular slip system rises with the increment in strain and is given by the extended Voce hardening law<sup>[45,46]</sup> as follows:

$$\tau_{\text{CRSS}}^s = \tau_0^s + (\tau_1^s + \theta_1^s \Gamma) \left( 1 - \exp\left(-\frac{\Gamma \theta_0^s}{\tau_1^s}\right) \right) \quad [\text{A3}]$$

Here,  $\tau_0^s$  is the initial CRSS;  $\tau_1^s$  is the back-extrapolated shear stress;  $\theta_0^s$  and  $\theta_1^s$  are the initial and asymptotic hardening rates and  $\Gamma = \int \sum_s d\gamma^s$  is the accumulated shear strain in the grain.

Further, the linearization of Eq. (A1) within the framework of the grain gives

$$\dot{\epsilon}_{ij} = \left\{ \dot{\gamma}_0 \sum_s \frac{m_{ij}^s m_{kl}^s}{\tau_{\text{CRSS}}^s} \left[ \frac{m_{kl}^s \sigma_{kl}}{\tau_{\text{CRSS}}^s} \right]^{n-1} \right\} \sigma_{kl} = M_{ijkl} \sigma_{kl} \quad [\text{A4}]$$

Here,  $M_{ijkl}$  is the viscoplastic compliance modulus of the grain. Similarly, at macroscopic level, the average response of a polycrystal represented by HEM [Figure 1(a)] can be described as follows:

$$\dot{\epsilon}^{\text{ag}} = \overline{\mathbf{M}} : \sigma^{\text{ag}} \quad [\text{A5}]$$

where  $\dot{\epsilon}^{\text{ag}}$  and  $\sigma^{\text{ag}}$  are the macroscopic strain rate and stress state of HEM, respectively;  $\overline{\mathbf{M}}$  is the macroscopic compliance moduli. The heart of the VPSC model resides in the following localization equation that describes the interaction of the inhomogeneous inclusion with the surrounding HEM medium.

$$\dot{\epsilon} - \dot{\epsilon}^{\text{ag}} = \mathbf{n}(\mathbf{I} - \mathbf{E})^{-1} : \mathbf{E} : \overline{\mathbf{M}} : (\sigma - \sigma^{\text{ag}}) \quad [\text{A6}]$$

where  $\mathbf{I}$  is the identity matrix and  $\mathbf{E}$  is the Eshelby tensor. The VPSC supports the implementation of various linearization schemes to describe the grain level interaction. The  $\mathbf{n}$  is the tuning parameter that controls this behavior, which ranges between two extreme values of 0 and  $\infty$ . From Eq. (A6), if  $\mathbf{n} = 0$ , then the grain scale strain rates are equal to the macroscopic ones describing the iso-strain Taylor theory. If  $\mathbf{n} = \infty$ , the grain scale stress state is equal to the macroscopic stress state, indicating the iso-stress Sachs model. In general, neither Taylor's nor Sachs's theory is entirely followed by the deforming material, and correspondingly intermediate  $\mathbf{n}$  values are prescribed that are more suitable. Different intermediate schemes like secant ( $\mathbf{n} = 1$ ), tangent ( $\mathbf{n} = 20$ ), and  $n^{\text{eff}}$  ( $\mathbf{n} = 10$ ) are available in the VPSC code for describing the interaction of the grain with the HEM medium. Finally, in the VPSC, iterations are performed at each step of the simulation such that the self-consistency is maintained. It explains that the stress and strain rate states of individual grains are allowed to vary, but their average response should be consistent with the macroscopic ones. Correspondingly, the lattice reorientation and the change in the shape of the grain (*i.e.*, inclusion) are updated at each incremental strain during simulation.

## REFERENCES

1. S. Floreen, G.E. Fuchs, and W.J. Yang: *Superalloys 718,625,706 and Various Derivatives*, Proceedings of the Third International Special Emphasis Symposium, The Minerals, Metals & Materials Society, Pittsburgh, Pennsylvania, June 27–29, 1994, pp. 13–37.
2. R.M.F. Jones and L.A. Jackman: *JOM*, 1999, vol. 51, pp. 27–33.

3. A.K. Godasu, U. Prakash, and S. Mula: *J. Alloys Compd.*, 2020, vol. 844, p. 156200.
4. D. Li, Q. Guo, S. Guo, H. Peng, and Z. Wu: *Mater. Des.*, 2011, vol. 32, pp. 696–705.
5. J. Hirsch and K. Lücke: *Acta Metall.*, 1988, vol. 36, pp. 2863–82.
6. O. Engler: *Acta Mater.*, 2000, vol. 48, pp. 4827–40.
7. R. Madhavan, R.K. Ray, and S. Suwas: *Philos. Mag.*, 2016, vol. 96, pp. 3177–199.
8. C. Donadille, R. Valle, P. Dervin, and R. Penelle: *Acta Metall.*, 1989, vol. 37, pp. 1547–71.
9. S. Suwas and R.K. Ray: *Crystallographic Texture of Materials*, Springer, London, 2014.
10. B.J. Duggan, M. Hatherly, W.B. Hutchinson, and P.T. Wakefield: *Met. Sci.*, 1978, vol. 12, pp. 343–51.
11. T. Leffers and R.K. Ray: *Prog. Mater. Sci.*, 2009, vol. 54, pp. 351–96.
12. I.L. Dillamore: *Metall. Trans.*, 1970, vol. 1, pp. 2463–70.
13. W. Heye and G. Wassermann: *Scripta Metall.*, 1968, vol. 2, pp. 205–07.
14. T. Leffers and J.B. Bilde-Sørensen: *Acta Metall. Mater.*, 1990, vol. 38, pp. 1917–26.
15. P. Van Houtte: *Acta Metall.*, 1978, vol. 26, pp. 591–604.
16. S.R. Kalidindi: *J. Mech. Phys. Solids*, 1998, vol. 46, pp. 267–71.
17. M. Hatherly and A.S. Malin: *Scripta Metall.*, 1984, vol. 18, pp. 449–54.
18. A. Rollett, F. Humphreys, G.S. Rohrer, and M. Hatherly: *Recrystallization and Related Annealing Phenomena*, 2nd ed. Elsevier Ltd, Amsterdam, 2004.
19. R. Madhavan, R.K. Ray, and S. Suwas: *Acta Mater.*, 2014, vol. 74, pp. 151–64.
20. A.K. Godasu, S. Mishra, U. Prakash, and S. Mula: *Metall. Mater. Trans. A*, 2022, vol. 53A, pp. 2239–58.
21. F. Bachmann, R. Hielscher, and H. Schaeben: *Solid State Phenom.*, 2010, vol. 160, pp. 63–68.
22. A. Molinari, G.R. Canova, and S. Ahzi: *Acta Metall.*, 1987, vol. 35, pp. 2983–94.
23. R.A. Lebensohn and C.N. Tomé: *Acta Metall. Mater.*, 1993, vol. 41, pp. 2611–24.
24. N.P. Gurao and S. Suwas: *Mater. Lett.*, 2013, vol. 99, pp. 81–85.
25. A.K. Ray: Doctoral Dissertation, Queen's University, Kingston, 2009.
26. D.A. Hughes, N. Hansen, and D.J. Bammann: *Scripta Mater.*, 2003, vol. 48, pp. 147–53.
27. L.S. Tóth, Y. Estrin, R. Lapovok, and C. Gu: *Acta Mater.*, 2010, vol. 58, pp. 1782–94.
28. D. Kuhlmann-Wilsdorf and N. Hansen: *Scripta Metall. Mater.*, 1991, vol. 25, pp. 1557–62.
29. I.L. Dillamore, J.G. Roberts, and A.C. Bush: *Met. Sci.*, 1979, vol. 13, pp. 73–77.
30. P. Wagner, O. Engler, and K. Lucke: *Acta Metall. Mater.*, 1995, vol. 43, pp. 3799–812.
31. L.S. Toth, C.F. Gu, B. Beausir, J.J. Fundenberger, and M. Hoffman: *Acta Mater.*, 2016, vol. 117, pp. 35–42.
32. L. Anand and S.R. Kalidindi: *Mech. Mater.*, 1994, vol. 17, pp. 223–43.
33. N. Jia, P. Eisenlohr, F. Roters, D. Raabe, and X. Zhao: *Acta Mater.*, 2012, vol. 60, pp. 3415–34.
34. I.L. Dillamore and W.T. Roberts: *Acta Metall.*, 1964, vol. 12, pp. 281–93.
35. D. Raabe, Z. Zhao, S.J. Park, and F. Roters: *Acta Mater.*, 2002, vol. 50, pp. 421–40.
36. B. Geddes, H. Leon, and X. Huang: *Superalloys Alloying and Performance*, 1st ed., ASM International, 2009, pp. 1–176.
37. K. Morii, H. Mecking, and Y. Nakayama: *Acta Metall.*, 1985, vol. 33, pp. 379–86.
38. M. Ferry and F.J. Humphreys: *Mater. Sci. Eng. A*, 2006, vol. 436, pp. 447–52.
39. H. Paul, C. Maurice, and J.H. Driver: *Acta Mater.*, 2010, vol. 58, pp. 2799–813.
40. R. Becker: *J. Mech. Phys. Solids*, 1991, vol. 39, pp. 459–76.
41. J. Hirsch and K. Lücke: *Acta Metall.*, 1988, vol. 36, pp. 2883–904.
42. J. Hirsch, K. Lücke, and M. Hatherly: *Acta Metall.*, 1988, vol. 36, pp. 2905–27.
43. C.D. Singh, V. Ramaswamy, and C. Suryanarayana: *Textures Microstruct.*, 1992, vol. 19, pp. 101–21.

44. O. Engler, M.Y. Huh, and C.N. Tomé: *Metall. Mater. Trans. A*, 2000, vol. 31A, pp. 2299–15.
45. C. Tome, G.R. Canova, U.F. Kocks, N. Christodoulou, and J.J. Jonas: *Acta Metall.*, 1984, vol. 32, pp. 1637–53.
46. C.N. Tome and R.A. Lebensohn: *Visco-Plastic Self-Consistent (VPSC)*, Los Alamos National Laboratory, Universidad Nacional de Rosario, Los Alamos, Rosario, 2009.

**Publisher's Note** Springer Nature remains neutral with regard to jurisdictional claims in published maps and institutional affiliations.

Springer Nature or its licensor (e.g. a society or other partner) holds exclusive rights to this article under a publishing agreement with the author(s) or other rightsholder(s); author self-archiving of the accepted manuscript version of this article is solely governed by the terms of such publishing agreement and applicable law.